Two-Phase Approach to Modeling the Grain-Fluid Flows with Deposition and Entrainment over Rugged Topography

Hock-Kiet Wong[1], **Yih-Chin Tai**[1], **Haruka Tsunetaka**[2], **Norifumi Hotta**[3]

[1]Department of Hydraulic and Ocean Engineering, National Cheng Kung University, Tainan, Taiwan.
[2]Forestry and Forest Products Research Institute, Ibaraki, Japan
[3]Graduate School of Agricultural and Life Sciences, The University of Tokyo, Tokyo, Japan

Key Points:

- A two-phase mixture model for debris flows over erodible and rugged topography is proposed.
- In the model, entrainment is induced by the basal shear stress and deposition takes place mainly due to the sediment settling process.
- In addition to the significant impacts on the post-event morphology, levee formation and layered deposits can be reproduced.

Corresponding author: Yih-Chin Tai, `yctai@ncku.edu.tw`

Abstract

We present a grain-fluid mixture for debris flows moving on a rugged (non-trivial) topography, where entrainment and deposition may take place. The model equations are derived with respect to a terrain-following coordinate system, which is constructed based on the topographic surface. The coordinates are fixed in space, and a ”subtopography” is added on the coordinate surface to account for the variation in the local topography when entrainment or deposition takes place. Numerical implementation is made based on a GPU-accelerated simulation tool, into which the entrainment-deposition mechanism is integrated accordingly. Two numerical examples are assigned to investigate the key features of the proposed model. One is on a horizontal plane, on which a finite mass of grain-fluid mixture is released from the state of rest. In this example, debris flow deposits significantly impact the post-event morphology and the associated flow behaviors. The other concerns a moving mass down an inclined chute merging into a horizontal deposition plane, where the levee formation is reproduced. At the end, the model is validated against a debris flow experiment to evaluate its applicability.

Plain Language Summary

Debris flows are grain-fluid mixtures driven by gravity and moving in mountain areas. Generally, they deposit when entering the open area with gentle slopes, which is commonly either the agricultural regions or the residential areas. Because of their high density, debris flows threaten residents and destroy infrastructure, and the deposited material may bury farms and buildings. In the post-event surveys, a large difference between the initial volume and the deposit heap can often be identified, indicating entrainment on the flow paths during movement. In this study, we present a grain-fluid mixture for debris flows moving on rugged topography. The introduction of the entrainment-deposition process allows the dynamic evolution of the deposit heap to be described, and levee formation can be reproduced. Using two numerical examples, we confirm the impacts of the entrainment-deposition process on the flow behaviors and the deposit morphology. The applicability of the present model is validated by outdoor debris flow experiments.

1 Introduction

Debris flows are grain-fluid mixtures driven by gravity and moving in mountain areas (e.g., Hutter et al., 1996; Takahashi, 2007). Generally, they deposit in areas with gentle slopes, which usually are either agricultural regions or residential areas. Although the speed has decreased in the deposition area, the debris flows are still highly destructive and threaten residents and infrastructure due to the severe impacts of the high-density flows. The deposited material may bury farms, houses and associated infrastructure. Post-event measurements sometimes indicate a large difference between the initial volume and the final deposits, giving solid evidence of entrainment on the flow paths (e.g., Pierson et al., 1990; Hungr et al., 2005; Chen et al., 2006, 2012, 2014; Berger et al., 2010). In some circumstances, the entrained or deposited material may change the composition of the debris flow, increasing the complexity of determining the rheology. Hence, addressing the varying rheology during movement with a single-phase approach is highly challenging.

Numerical simulations for scenario investigation can be employed as a powerful tool to estimate the debris flow hazard area. Many numerical simulation tools have been developed based on depth-averaged models to improve the computational efficiency because the assessments generally cover large areas. However, the coordinate system used may play an important role in depth-averaged models because the depth-averaged velocities are parallel to the coordinate axes. High deviations may occur for highly rugged topography when the conventional Cartesian coordinate system is adopted. Hence, a terrain-following coordinate system is proposed (e.g., Bouchut & Westdickenberg, 2004; Tai &

Kuo, 2008; Tai et al., 2012; Luca et al., 2009), in which the axes coincide with the topographical surface. A comprehensive guidance for modeling gravity-driven flows sliding on rugged topography can be found in Luca et al. (2016).

Within the continuum-mechanical framework, the model equations for debris flows over erodible beds are generally derived and simplified with the depth-averaged approach. In addition, because the debris flows consist of grains and interstitial fluid, most models are based on the concept of mixture, and they can be approximately categorized into two types: quasi-two-phase and two-phase (or multiphase) approaches. Although the flow body should consist of solid and fluid phases in the quasi-two-phase approach, the relative velocity between the constituents is assumed to be very small compared with the barycentric velocity. Only the momentum balance for the entire mixture is considered. Consequently, only the barycentric velocity needs to be computed and no individual velocity for each constituent is available. The main drawback of the quasi-two-phase approach is the difficulty of describing the grain-fluid (phase) separation induced by the different velocities of the phases. In addition, addressing the variation in rheology caused by the change of the composition concentrations is also difficult. However, most entrainment-deposition rates are based on this quasi-two-phase approach, such as Takahashi et al. (1992); Pitman et al. (2003); Cao et al. (2004); Li and Duffy (2011); Tai and Kuo (2012) and Iverson and George (2014). Recently, Nishiguchi and Uchida (2022) noticed the importance of rheology variation and suggested the concept of "phase-shift" in modeling debris flows with the quasi-two-phase approach, where the associated impacts of the fine sediments on the flow dynamics are investigated with respect to a landslide-induced debris flow.

With the two-phase (or multiphase) approach, each constituent has its own velocity such that the grain-fluid separation can be well captured. Many of the two-phase models for debris flows are based on the pioneering work of Pitman and Le (2005), and many extensions exist. For example, Pudasaini (2012) proposed a general two-phase model for debris flows. In Meng and Wang (2016), the buoyancy force is given in a different form for an appropriate expression in the static state. Tai et al. (2019) introduced the model equations of Meng and Wang (2016) in the terrain-following coordinates, and the non-hydrostatic pore-fluid pressure with nonlinear deformation of the granular skeleton is considered in Heß et al. (2019). In addition, with the two-phase approach, the dilatancy effects are considered in Bouchut et al. (2016, 2017). Multiphase (grain, fine sediments and water) models can be found in Pudasaini and Mergili (2019) and Ma et al. (2022). Although the above-mentioned models can address grain-fluid separation, they do not include the entrainment-deposition mechanism.

As elaborated in Pudasaini and Fischer (2020), entrainment-deposition rates specifically proposed for two-phase solid-fluid models are rare. In addition to the complexity of theoretical formulation, this problem is also fraught with the scarcity of reliable data in experiments for parameter calibration. For instance, while the entrainment-deposition rate can be approximated by analyzing the jump condition of the momentum balance equation at the basal interface using the ratio of the difference of the shear stress to the difference in velocities on either side of the interface (e.g., Fraccarollo & Capart, 2002; Iverson, 2012; Issler, 2014), there is a scarcity of corresponding experimental data. Measurements of the shear stresses for an erodible bed are rare, and the measurement of the velocity for granular flows is mainly limited to the near-wall field (e.g., Shirsath et al., 2015; Sarno et al., 2018). Nevertheless, Pudasaini and Fischer (2020) presented a mechanical two-phase erosion model in which the entrainment rates are considered for the solid and fluid phases separately and addressed five aspects for the entrainment-deposition rate in modeling geophysical mass flows. In addition to the continuum-mechanical approach, Suzuki and Hotta (2016) employed a particle method for simulating debris flows, the Modified Particles Method (MPS), where the entrainment-deposition process is included at the basal surface. Suzuki et al. (2019) extended this MPS method to 3D and applied it to mimic the depositional process of alluvial fans in experiments. In Suzuki et al. (2019), the entrainment-deposition rate follows the suggestion in Suzuki et al. (2009), where the concept of the equilibrium sediment concentration (cf. Egashira, 1997) is adopted.

In the present study, erosion (entrainment) and deposition are considered to be based on distinct mechanisms: erosion is basically induced by the basal shear stress, and deposition takes place mainly due to the process of sediment settling. This concept stems from Cao et al. (2004) and Li and Duffy (2011), which are based on quasi-two-phase models. Here, we extend their concept for flows in a two-phase approach. In the new entrainment and deposition mechanisms, the Shields parameter (Shields, 1936) and the Hjulström-Sundborg diagram (Hjulström, 1935) are considered for the initiations of entrainment and deposition, respectively. All model equations are derived in terrain-following coordinates (cf. Tai et al., 2012; Luca et al., 2016). In addition, following Tai et al. (2012) and Tai and Kuo (2012), the momentum loss due to deposition is considered, while no momentum gain occurs due to the entrainment because the eroded material is at rest in the bed before being entrained. Numerical implementation is achieved with a high-resolution shock-capturing scheme, the anti-diffusive, nonoscillatory central scheme proposed by Kurganov and Tadmor (2000) and Kurganov and Petrova (2007). With the integration of the present model into the GPU-accelerated simulation tool (MoSES_2PDF in Ko et al. (2021)), the computational efficiency is highly enhanced for scenario investigations and/or parameter calibration. Two idealized topographies (horizontal plane and inclined curved chute) are assigned to investigate and highlight the key features caused by the introduction of entrainment/deposition, where its impacts on the morphology and flow behaviors are examined. On the horizontal plane, a finite mass of grain-fluid mixture is released from the state of rest, and the material subsequently deposits on the plane. In the example of inclined curved chute, the flow body slides down the inclined section merging into a horizontal deposition plane. In addition to idealized numerical examples, the present model is validated against debris flow experiments shown in Suzuki et al. (2019) and Tsunetaka et al. (2022).

The remainder of this paper is structured as follows. In section 2, we provide a brief introduction to the resultant equations of the proposed grain-fluid model with entrainment and deposition, where the flow body is treated as a fully saturated mixture. Two numerical examples and one experimental validation are numerically investigated in section 3, in which the key features and applicability of the proposed model are thoroughly examined. Finally, concluding remarks and perspectives are given in section 4.

2 Model equations

2.1 Two-Phase Grain-Fluid Model Equations

The model used in the present study is based on Tai et al. (2019), where the model equations are derived using a depth-averaged approach and presented in dimensionless form. A terrain-following coordinate system (cf. Tai & Kuo, 2012; Tai et al., 2012; Luca et al., 2012, 2016) is employed in the derivation. As shown in Fig. 1, the flow depth is defined in the normal ζ-direction, and the ξ- and η-coordinates are tangential to the basal surface, where the ζ-direction coincides with the unit normal vector $\boldsymbol{n} = n_x\mathbf{e}_x + n_y\mathbf{e}_y + n_z\mathbf{e}_z$ of the basal surface. Letting $\boldsymbol{r}_{xyz}$ and $\boldsymbol{r}_{\xi\eta\zeta}$ be the position vectors in O_{xyz} and $O_{\xi\eta\zeta}$, respectively, they are related by the Jacobian (transformation) matrix $\boldsymbol{\Omega}$, i.e., $\boldsymbol{r}_{xyz} = \boldsymbol{\Omega}\, \boldsymbol{r}_{\xi\eta\zeta}$. The flow body is assumed to be shallow, i.e., a characteristic length $\mathcal{L}$ of the flow body along the topographic surface and a respective characteristic flow thickness $\mathcal{H}$, where the aspect ratio $\epsilon = \mathcal{H}/\mathcal{L} \ll 1$ is small. As elaborated in Tai et al. (2019), we use $\boldsymbol{\Omega} = \boldsymbol{\Omega}_\mathrm{b} + \mathcal{O}(\epsilon^\chi)$ with $\chi \in (0, 1)$ for a topographic surface of shallow curvature, where $\boldsymbol{\Omega}_\mathrm{b}$ is the Jacobian matrix (transformation of coordinates) for the basal surface. The two-phase approach gives two equations for the mass balance and six equations for momentum conservation in three-dimensional configuration. The depth-integration process reduces the number of momentum equations from six to four. With the aid of scaling anal-

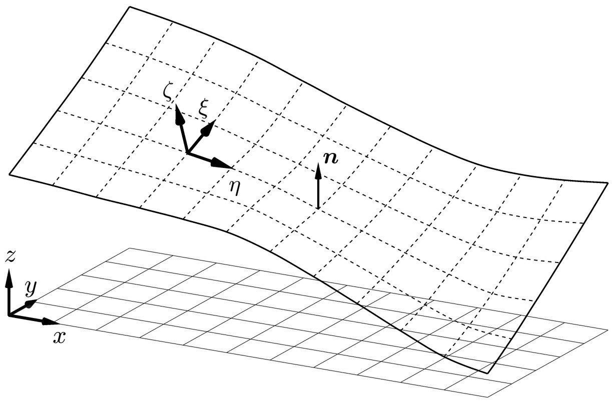

Figure 1. Coordinate system O_{xyz} and $O_{\xi\eta\zeta}$, in which the ζ-direction coincides with the unit normal vector $\boldsymbol{n} = (n_x, n_y, n_z)$ in O_{xyz}.

ysis, all physically insignificant terms are isolated in the resultant model equations (see e.g. Tai et al., 2019).

The model equations are similar to the ones listed in (Tai et al., 2019). For ease of distinguishing the differences, the additional terms and equation are marked in blue. With $J_\mathrm{b} = \det \boldsymbol{\Omega}_\mathrm{b}$, the resultant mass balance equations for the solid and fluid phases are

$$\frac{\partial}{\partial t}(J_\mathrm{b} h^\mathrm{s}) + \frac{\partial}{\partial \xi}(J_\mathrm{b} h^\mathrm{s} v^\mathrm{s}_\xi) + \frac{\partial}{\partial \eta}(J_\mathrm{b} h^\mathrm{s} v^\mathrm{s}_\eta) = J_\mathrm{b} \mathcal{E}^\mathrm{s} \tag{1}$$

and

$$\frac{\partial}{\partial t}(J_\mathrm{b} h^\mathrm{f}) + \frac{\partial}{\partial \xi}(J_\mathrm{b} h^\mathrm{f} v^\mathrm{f}_\xi) + \frac{\partial}{\partial \eta}(J_\mathrm{b} h^\mathrm{f} v^\mathrm{f}_\eta) = J_\mathrm{b} \mathcal{E}^\mathrm{f} \,, \tag{2}$$

respectively. In (1) and (2), $h^\mathrm{s} = h\phi^\mathrm{s}$ and $h^\mathrm{f} = h\phi^\mathrm{f}$, with h representing the mixture total depth, ϕ^s and ϕ^f denoting the depth-averaged volume concentrations of the solid and fluid phases, respectively, $v_{\xi,\eta}$ is the tangential component of the depth-averaged velocity in the terrain-following coordinate system, and $\mathcal{E}^\mathrm{s,f}$ represent the entrainment rates of the solid and fluid phases. Here, the deposit is assumed to be fully saturated during the depositional process, yielding $\mathcal{E}^\mathrm{f} = \mathcal{E}^\mathrm{s}\phi^\mathrm{f}_\mathrm{b}/(1-\phi^\mathrm{f}_\mathrm{b})$, where $\phi^\mathrm{f}_\mathrm{b}$ is the porosity of the erodible bed. Hence, the evolution of the deposit heap is given by

$$\frac{\partial \zeta_\mathrm{b}}{\partial t} = \frac{\mathcal{E}^\mathrm{s}}{\phi^\mathrm{s}_\mathrm{b}} = \frac{\mathcal{E}^\mathrm{f}}{\phi^\mathrm{f}_\mathrm{b}} \quad \text{with} \quad \phi^\mathrm{s}_\mathrm{b} + \phi^\mathrm{f}_\mathrm{b} = 1\,. \tag{3}$$

The depth-averaged, leading-order momentum equations of the solid phase are given by

$$\begin{aligned} &\frac{\partial}{\partial t}\left(J_\mathrm{b} h^\mathrm{s} v^\mathrm{s}_x\right) + \frac{\partial}{\partial \xi}\Big(J_\mathrm{b} h^\mathrm{s} v^\mathrm{s}_x v^\mathrm{s}_\xi + \epsilon J_\mathrm{b} h A_{11} \overline{N}^\mathrm{s}\Big) + \frac{\partial}{\partial \eta}\Big(J_\mathrm{b} h^\mathrm{s} v^\mathrm{s}_x v^\mathrm{s}_\eta + \epsilon J_\mathrm{b} h A_{21} \overline{N}^\mathrm{s}\Big) \\ &\quad = \underbrace{J_\mathrm{b} p^\mathrm{s}_\mathrm{b} n_x}_{\text{(i)}} - \epsilon \alpha_\rho F^\mathrm{B}_{1121} + J_\mathrm{b} \alpha_\rho F^\mathrm{Rel}_x - \underbrace{\epsilon J_\mathrm{b} \Big\{ N^\mathrm{s}_\mathrm{b} + \alpha_\rho \phi^\mathrm{s} N^\mathrm{f}_\mathrm{b} \Big\} \Phi_{1121}}_{\text{(ii)}} \\ &\qquad - \underbrace{J_\mathrm{b} p^\mathrm{s}_\mathrm{b} \tan\delta_\mathrm{b} \frac{v^\mathrm{s}_x}{\|\mathbf{v}^\mathrm{s}\|}}_{\text{(iii)}} + \underbrace{J_\mathrm{b} v^\mathrm{s}_{x,\mathrm{b}} \mathcal{E}^\mathrm{s}}_{\text{(iv)}} \end{aligned} \tag{4}$$

and

$$
\begin{aligned}
&\frac{\partial}{\partial t}\left(J_{\rm b}h^{\rm s}v_y^{\rm s}\right)+\frac{\partial}{\partial \xi}\Big(J_{\rm b}h^{\rm s}v_y^{\rm s}v_\xi^{\rm s}+\epsilon J_{\rm b}hA_{12}\overline{N}^{\rm s}\Big)+\frac{\partial}{\partial \eta}\Big(J_{\rm b}h^{\rm s}v_y^{\rm s}v_\eta^{\rm s}+\epsilon J_{\rm b}hA_{22}\overline{N}^{\rm s}\Big)\\
&\quad=\underbrace{J_{\rm b}p_{\rm b}^{\rm s}n_y}_{\rm (i)}-\epsilon\alpha_\rho F_{1222}^{\rm B}+J_{\rm b}\alpha_\rho F_y^{\rm Rel}-\underbrace{\epsilon J_{\rm b}\Big\{N_{\rm b}^{\rm s}+\alpha_\rho\phi^{\rm s}N_{\rm b}^{\rm f}\Big\}\Phi_{1222}}_{\rm (ii)}\\
&\qquad\underbrace{-\,J_{\rm b}p_{\rm b}^{\rm s}\tan\delta_{\rm b}\frac{v_y^{\rm s}}{\|\mathbf{v}^{\rm s}\|}}_{\rm (iii)}+\underbrace{J_{\rm b}v_{y,{\rm b}}^{\rm s}\mathcal{E}^{\rm s}}_{\rm (iv)},
\end{aligned}
\tag{5}
$$

where, with $\partial_\xi(\cdot)=\partial(\cdot)/\partial\xi$ and $\partial_\eta(\cdot)=\partial(\cdot)/\partial\eta$,

$$
\begin{aligned}
&F_{1121}^{\rm B}=\phi^{\rm s}\Big\{A_{11}\partial_\xi(J_{\rm b}h\overline{p}^{\rm f})+A_{21}\partial_\eta(J_{\rm b}h\overline{p}^{\rm f})\Big\},\\
&F_{1222}^{\rm B}=\phi^{\rm s}\Big\{A_{12}\partial_\xi(J_{\rm b}h\overline{p}^{\rm f})+A_{22}\partial_\eta(J_{\rm b}h\overline{p}^{\rm f})\Big\},\\
&F_x^{\rm Rel}=c_D\phi^{\rm s}\phi^{\rm f}h(v_x^{\rm f}-v_x^{\rm s}),\qquad F_y^{\rm Rel}=c_D\phi^{\rm s}\phi^{\rm f}h(v_y^{\rm f}-v_y^{\rm s}),
\end{aligned}
\tag{6}
$$

and

$$
\Phi_{1121}=A_{11}\partial_\xi\zeta_{\rm b}+A_{21}\partial_\eta\zeta_{\rm b}\,,\qquad \Phi_{1222}=A_{12}\partial_\xi\zeta_{\rm b}+A_{22}\partial_\eta\zeta_{\rm b}
\tag{7}
$$

are introduced. In (4) – (7), $\mathbf{A}=(A_{ij})=\mathbf{\Omega}_{\rm b}^{-1}$, and $\alpha_\rho(=\rho^{\rm f}/\rho^{\rm s})$ stands for the density ratio of flowing body. $\overline{N}^{\rm s}=n_z(1-\alpha_\rho)h^{\rm s}/2$ and $\overline{p}^{\rm f}=n_zh/2$ respectively denote the depth-averaged pressure of the solid and fluid phase. Notation $p_{\rm b}^{\rm s}=h^{\rm s}n_z[(1-\alpha_\rho)-\epsilon^\chi\kappa^{\rm s}]$ represents the solid pressure at the basal surface, where $\kappa^{\rm s}=v_x^{\rm s}(\partial_\xi n_x)v_\xi^{\rm s}+v_\xi^{\rm s}(\partial_\xi n_y)v_y^{\rm s}+v_\xi^{\rm s}(\partial_\xi n_z)v_z^{\rm s}+v_\eta^{\rm s}(\partial_\eta n_x)v_x^{\rm s}+v_\eta^{\rm s}(\partial_\eta n_y)v_y^{\rm s}+v_\eta^{\rm s}(\partial_\eta n_z)v_z^{\rm s}$ represents the centripetal acceleration (cf. Tai et al., 2012, 2019). Notations $F_{1121/1222}^{\rm B}$ denote the buoyancy forces, $F_{x/y}^{\rm Rel}$ stand for the drags due to the velocity difference between the two phases, and c_D is the drag (between the constituents) coefficient. On the right-hand side of (4) and (5), terms (i) are the components of the normal pressure at the bottom, which are caused by the reaction force of gravity; terms (ii) represent the effects caused by the deposit heap; terms (iii) indicate the basal drags with $\delta_{\rm b}$ being the angle of basal friction of the solid phase; terms (iv) stand for the momentum loss due to deposition.

The momentum equations for the fluid phase read as

$$
\begin{aligned}
&\frac{\partial}{\partial t}(J_{\rm b}h^{\rm f}v_x^{\rm f})+\frac{\partial}{\partial \xi}(J_{\rm b}h^{\rm f}v_x^{\rm f}v_\xi^{\rm f}+\epsilon J_{\rm b}hA_{11}\overline{p}^{\rm f})+\frac{\partial}{\partial \eta}(J_{\rm b}h^{\rm f}v_x^{\rm f}v_\eta^{\rm f}+\epsilon J_{\rm b}hA_{21}\overline{p}^{\rm f})\\
&\quad=\underbrace{J_{\rm b}p_{\rm b}^{\rm f}n_x}_{\rm (v)}+\epsilon F_{1121}^{\rm B}-J_{\rm b}F_x^{\rm Rel}+\epsilon F_x^{\rm Vis}\underbrace{-J_{\rm b}h^{\rm f}\frac{\vartheta_{\rm b}^{\rm f}v_x^{\rm f}}{\epsilon N_R}-J_{\rm b}\Pi^{\rm M}\frac{n^2h^{\rm f}v_x^{\rm f}\|\boldsymbol{v}^{\rm f}\|}{h^{{\rm f}\,4/3}}}_{\rm (vi)}\\
&\qquad-\underbrace{\epsilon J_{\rm b}\phi^{\rm f}N_{\rm b}^{\rm f}\Phi_{1121}}_{\rm (vii)}+\underbrace{J_{\rm b}v_{x,{\rm b}}^{\rm f}\mathcal{E}^{\rm f}}_{\rm (viii)}
\end{aligned}
\tag{8}
$$

in the x-direction, and

$$
\begin{aligned}
&\frac{\partial}{\partial t}(J_{\rm b}h^{\rm f}v_y^{\rm f})+\frac{\partial}{\partial \xi}(J_{\rm b}h^{\rm f}v_y^{\rm f}v_\xi^{\rm f}+\epsilon J_{\rm b}hA_{12}\overline{p}^{\rm f})+\frac{\partial}{\partial \eta}(J_{\rm b}h^{\rm f}v_x^{\rm f}v_\eta^{\rm f}+\epsilon J_{\rm b}hA_{22}\overline{p}^{\rm f})\\
&\quad=\underbrace{J_{\rm b}p_{\rm b}^{\rm f}n_y}_{\rm (v)}+\epsilon F_{1222}^{\rm B}-J_{\rm b}F_y^{\rm Rel}+\epsilon F_y^{\rm Vis}\underbrace{-J_{\rm b}h^{\rm f}\frac{\vartheta_{\rm b}^{\rm f}v_y^{\rm f}}{\epsilon N_R}-J_{\rm b}\Pi^{\rm M}\frac{n^2h^{\rm f}v_y^{\rm f}\|\boldsymbol{v}^{\rm f}\|}{h^{{\rm f}\,4/3}}}_{\rm (vi)}\\
&\qquad-\underbrace{\epsilon J_{\rm b}\phi^{\rm f}N_{\rm b}^{\rm f}\Phi_{1222}}_{\rm (vii)}+\underbrace{J_{\rm b}v_{y,{\rm b}}^{\rm f}\mathcal{E}^{\rm f}}_{\rm (viii)},
\end{aligned}
\tag{9}
$$

in the y-direction, where we introduce

$$
\begin{aligned}
F_x^{\mathrm{Vis}} = \frac{\phi^{\mathrm{f}}}{N_R} \Big\{ & 2\partial_\xi \Big[J_{\mathrm{b}} h \left(A_{11}\partial_\xi v_\xi^{\mathrm{f}} + A_{21}\partial_\eta v_\xi^{\mathrm{f}} \right) \Big] \\
& + \partial_\eta \Big[J_{\mathrm{b}} h \big(A_{12}\partial_\xi v_\xi^{\mathrm{f}} + A_{22}\partial_\eta v_\xi^{\mathrm{f}} + A_{11}\partial_\xi v_\eta^{\mathrm{f}} + A_{21}\partial_\eta v_\eta^{\mathrm{f}} \big) \Big] \Big\} \\
F_y^{\mathrm{Vis}} = \frac{\phi^{\mathrm{f}}}{N_R} \Big\{ & \partial_\xi \Big[J_{\mathrm{b}} h \left(A_{12}\partial_\xi v_\xi^{\mathrm{f}} + A_{22}\partial_\eta v_\xi^{\mathrm{f}} + A_{11}\partial_\xi v_\eta^{\mathrm{f}} + A_{21}\partial_\eta v_\eta^{\mathrm{f}} \right) \Big] \\
& + 2\partial_\eta \Big[J_{\mathrm{b}} h \left(A_{12}\partial_\xi v_\eta^{\mathrm{f}} + A_{22}\partial_\eta v_\eta^{\mathrm{f}} \right) \Big] \Big\}
\end{aligned}
\tag{10}
$$

for the viscous effects with $N_R = \rho^{\mathrm{f}} \mathcal{H}\sqrt{g\mathcal{L}}/\mu^{\mathrm{f}}$ and μ^{f} the fluid viscosity (cf. Tai et al., 2019). On the right-hand side of (8) and (9), terms (v) indicate the components of the normal pressure at the bottom; terms (vi) are the basal drags; terms (vii) represent the effects caused by the deposit heap; and terms (viii) represent the momentum loss due to deposition. Notably, the basal drags indicated in terms (vi) consist of two terms, the first of which refers to the Navier drag as employed in Tai et al. (2019), and the second term accounts for the Manning drag, as widely applied in open channel flows (see e.g., Li & Duffy, 2011). In the Manning drag term, n is the Manning coefficient, and $\Pi^{\mathrm{M}} = \mathcal{H}^{4/3}/(g\,\mathcal{L})$ is a factor for the consistency of dimension.

In addition, the maximum value of the solid concentration must be limited in the range of $[0.6, 0.8]$ in the computation because the grains have their own shapes. However, when using the above model equations, the solid concentration may approach unity. Such a high value is unrealistic. Nevertheless, we also found that a large value of the drag coefficient c_D in (6) can alleviate the phase separation. In the present study, instead of a constant value, we suggest that

$$
c_D = c_{d0} \left\{ 1.0 + e^{\left[n_c\,(\phi^{\mathrm{s}} - 0.5)/\phi^{\mathrm{s}}_{\max} \right]} \right\}
\tag{11}
$$

to reduce the unrealistically high solid concentration. In (11), c_{d0} is a coefficient whose value is related to the resistance (inverse of the permeability) for viscous flows through a porous medium (e.g., Darcy's Law), and n_c is an empirical coefficient. The formulation (11) will synchronize the movements of the two constituents at high solid concentrations, impeding the phase separation and therefore lowering the maximum solid concentration in the computation. In our numerical tests, $n_c = 6.0$ can deliver satisfactory results, and this value is used for all computations in the following study.

2.2 Entrainment and Deposition

Here, based on the concept of Cao et al. (2004) and Li and Duffy (2011), we propose a modified entrainment-deposition rate for the two-phase approach

$$
\mathcal{E}^{\mathrm{s}} = E^{\mathrm{s}} - D^{\mathrm{s}}
\tag{12}
$$

with

$$
E^{\mathrm{s}} = \begin{cases} \alpha_{\mathrm{E}}\sqrt{gh}\left(\tilde{\Psi} - \tilde{\Psi}_{\mathrm{crt}}\right)\phi^{\mathrm{s}}_{\mathrm{b}}\,, & \text{for} \quad \tilde{\Psi} > \tilde{\Psi}_{\mathrm{crt}} \\ 0.0\,, & \text{otherwise} \end{cases}
\tag{13}
$$

for the entrainment and

$$
D^{\mathrm{s}} = \begin{cases} \alpha_{\mathrm{D}}\,\omega\left(\tilde{\Sigma}_{\mathrm{b}} - \tilde{\Sigma}_{\mathrm{crt}}\right), & \text{for} \quad \tilde{\Sigma}_{\mathrm{b}} > \tilde{\Sigma}_{\mathrm{crt}} \\ 0.0\,, & \text{otherwise} \end{cases}
\tag{14}
$$

for deposition. In (13), α_{E} denotes the entrainment coefficient, and

$$
\tilde{\Psi} = \frac{\tau_{\mathrm{b}}}{(\rho^{\mathrm{s}} - \rho^{\mathrm{f}})gd}
\tag{15}
$$

is related to the Shields parameter (Shields, 1936), where d indicates the sediment diameter and τ_b stands for the resultant basal friction (i.e., sum of the terms (iii) and (vi) of the model equations in Sect. 2.1). $\tilde{\Psi}_\mathrm{crt}$ is the critical value whose magnitude depends on the the particle diameter of the sediments (cf. Berenbrock & Tranmer, 2008). In the present study, we set $\tilde{\Psi}_\mathrm{crt} = 0.04$ for all numerical investigations since the mean grain size used in the experiment in Sect 3.3 is approximately 2.6 mm.

In (14), α_D is the deposition coefficient, $\tilde{\Sigma}_\mathrm{crt}$ is the critical value, and we suggest

$$\tilde{\Sigma}_\mathrm{b} = \left(\tilde{\mathrm{v}} - \frac{\|\mathbf{v}^\mathrm{s}\|}{\sqrt{g\,d}} \right) \phi^\mathrm{s}\,, \tag{16}$$

which introduces a sediment-diameter-dependent critical speed for the occurrence of deposition. That is, for large flow speeds and small sediment concentrations, $\tilde{\Sigma}_\mathrm{b}$ decreases, and no deposition takes place. $\tilde{\mathrm{v}}$ is the dimensionless critical speed, whose value depends on the mean diameter of the sediment and can be determined with the help of the Hjulström-Sundborg diagram (cf. Hjulström, 1935; Earle, 2015). Following the Hjulström-Sundborg diagram for a 2.6-mm grain of sand, the transportation zone approximately lies in the velocity range $[0.1, 0.6]$ m/s, yielding the range $[0.627, 3.7]$ for $\tilde{\mathrm{v}}$. In the present study, we set $\tilde{\mathrm{v}} = 1.6$ for grains with a mean size of 2.6 mm. In addition, the impacts of the fluid viscosity are considered through the sediment settling velocity ω, which is given by an empirical formula (Zhang, 1989), namely,

$$\omega = \sqrt{\left(\frac{13.95\,\mu^\mathrm{f}}{\rho^\mathrm{f}\,d} \right)^2 + 1.09\,g\,d \left(\frac{\rho^\mathrm{s}}{\rho^\mathrm{f}} - 1 \right)} - \frac{13.95\,\mu^\mathrm{f}}{\rho^\mathrm{f}\,d}, \tag{17}$$

as employed in models for sediment transport, such as Li and Duffy (2011) or Cao et al. (2004).

With identical scalings for the model equations, (1) – (5) and (8) – (9), we have the dimensionless entrainment-deposition rate

$$\mathcal{E}^{\mathrm{s}*} = E^{\mathrm{s}*} - D^{\mathrm{s}*}\,. \tag{18}$$

Here, we use the superscript $(\,)^*$ to denote the quantities after the scaling process. In (18), the dimensionless entrainment rate reads

$$E^{\mathrm{s}*} = \begin{cases} \alpha^*_\mathrm{E}\,\sqrt{h^*}\,\big(\tilde{\Psi}^* - \tilde{\Psi}^*_\mathrm{crt}\big)\phi^\mathrm{s}_\mathrm{b}\,, & \text{for} \quad \tilde{\Psi}^* > \tilde{\Psi}^*_\mathrm{crt} \\ 0.0\,, & \text{otherwise} \end{cases} \tag{19}$$

where $\alpha^*_\mathrm{E} = \epsilon^{-1/2}\alpha_\mathrm{E}$, $\tilde{\Psi}^*_\mathrm{crt} = \tilde{\Psi}_\mathrm{crt}$, $d = \mathcal{L}\,d^*$,

$$\tilde{\Psi}^* = \frac{(\mathrm{iii})^* + \alpha_\rho(\mathrm{vi})^*}{(1-\alpha_\rho)\,d^*}\,, \quad (\mathrm{iii})^* = p^{\mathrm{s}*}_\mathrm{b}\tan\delta_\mathrm{b} \quad \text{and} \quad (\mathrm{vi})^* = h^{\mathrm{f}*}\frac{\vartheta^\mathrm{f}_\mathrm{b}\,\|\boldsymbol{v}^{\mathrm{f}*}\|}{\epsilon N_R} + \Pi^\mathrm{M}\frac{n^2 h^{\mathrm{f}*}\|\boldsymbol{v}^{\mathrm{f}*}\|^2}{{h^{\mathrm{f}*}}^{4/3}}\,.$$

Furthermore, the dimensionless deposition rate is given by

$$D^{\mathrm{s}*} = \begin{cases} \alpha^*_\mathrm{D}\,\omega^*\left(\tilde{\Sigma}^*_\mathrm{b} - \tilde{\Sigma}^*_\mathrm{crt}\right), & \text{for} \quad \tilde{\Sigma}^*_\mathrm{b} > \tilde{\Sigma}^*_\mathrm{crt} \\ 0.0\,, & \text{otherwise} \end{cases} \tag{20}$$

with $\alpha^*_\mathrm{D} = \epsilon^{-3/2}\alpha_\mathrm{D}$,

$$\tilde{\Sigma}^*_\mathrm{b} = \left(\tilde{\mathrm{v}} - \frac{\|\mathbf{v}^{\mathrm{s}*}\|}{\sqrt{d^*}} \right)\phi^\mathrm{s} \quad \text{and} \quad \omega^* = \sqrt{\left(\frac{13.95}{N_R\,d^*} \right)^2 + 1.09\,\epsilon\,d^* \left(\frac{1-\alpha_\rho}{\alpha_\rho} \right)} - \frac{13.95}{N_R\,d^*}\,.$$

Here, we note that $(\tilde{\Sigma}_\mathrm{b}, \tilde{\Sigma}_\mathrm{crt}) = \sqrt{\mathcal{L}/\mathcal{H}}\,\left(\tilde{\Sigma}^*_\mathrm{b}, \tilde{\Sigma}^*_\mathrm{crt}\right)$ and $\omega = \sqrt{g\mathcal{L}}\,\omega^*$.

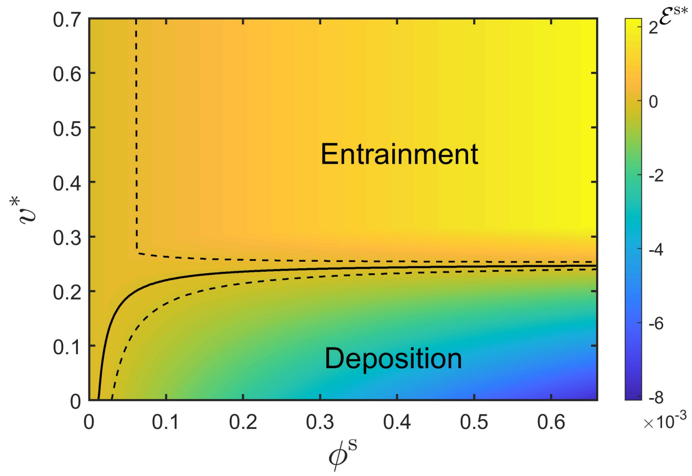

Figure 2. The resulting entrainment-deposition rate $\mathcal{E}^{\mathrm{s}*}$, plotted against v^* and ϕ^{s} for a flow thickness $h^* = 1.0$. The solid line represents the boundary between entrainment and deposition, while the dashed lines indicate the locations of $\mathcal{E}^{\mathrm{s}*} = \pm 2 \times 10^{-4}$, respectively.

The present formulation (18) (or (12)) provides a smooth transition between entrainment and deposition. Figure 2 depicts the resulting entrainment-deposition rate $\mathcal{E}^{\mathrm{s}*}$, computed by (18) for a flow thickness $h^* = 1.0$ with a mean sediment grain size of 0.026. The parameter values used are identical to those used in the numerical investigation (Sect. 3) and are listed in Table 1. The solid line in the graph represents the boundary between entrainment and deposition. The entrainment-deposition phenomenon is not significant when it lies within the area between the two dashed lines, which indicate the locations of $\mathcal{E}^{\mathrm{s}*} = \pm 2 \times 10^{-4}$ (about 0.02% of the flow thickness h^*). As shown in Fig. 2, entrainment dominates the process at high speed, and its magnitude increases gently with the speed. Deposition becomes dominant as the flow speed decreases and approaches zero. For very low solid concentration (e.g. $\phi^{\mathrm{s}} < 0.01$), neither entrainment nor deposition takes place.

3 Numerical Investigation

The equation system consists of (1) – (5), (8) – (9) together with (11) and (18), has been implemented and integrated into a CUDA-GPU-accelerated simulation tool called MoSES_2PDF, which is proposed by Ko et al. (2021). MoSES_2PDF is build on the foundation of the two-phase model by Tai et al. (2019) and developed using the anti-diffusive, nonoscillatory central scheme proposed by Kurganov and Tadmor (2000) and Kurganov and Petrova (2007). For high resolution in space, the Mimod TVD slope limiter is used for cell reconstruction. Kurganov and Tadmor (2000) proved that the Courant-Friedrichs-Lewy (CFL) number should be less than 0.125 to satisfy the *maximum principle*; consequently, CFL = 0.1 is set for all the following examples in the computation.

Two idealized numerical examples are available to explore the key features, and one experimental validation is available to examine the applicability. In the first idealized example (cf. Sect. 3.1), a heap with a parabolic shape in section view is released on a horizontal plane. The second example concerns a finite mass flowing down an inclined curved chute and merging into a horizontal deposition zone. In both examples, scenarios with and without the depositional mechanism are considered in the computation to investigate the impacts of the deposition mechanism on the flow behaviors. For the validation, we consider the debris flow experiment and the associated measurements and

Table 1. Parameters in computation for examples of horizontal flat plane and inclined curved chute

Parameters	Value	Description
$\epsilon = \mathcal{H}/\mathcal{L}$	1	Aspect Ratio
$\alpha_\rho = \rho^{\mathrm{f}}/\rho^{\mathrm{s}}$	0.4	Density Ratio (1.06/2.65)
ϕ_0^{s}	0.5	Initial solid concentration
δ_{b}	$35°$	Angle of basal friction (solid phase)
$\vartheta_{\mathrm{b}}^{\mathrm{f}}$	1.0	Navier fluid friction coefficient
c_{d0}	4.0	Drag coefficient
μ^{f}	$3.5\ \mathrm{mPa \cdot s}$	Viscosity of interstitial fluid
N_R	30,000	Viscous number
d^*	0.026	Sediment median diameter
$\tilde{\Psi}_{\mathrm{crt}}^*$	0.04	Critical Shields parameter
$\tilde{\mathrm{v}}$	2.0	Dimensionless critical speed for deposition
$\tilde{\Sigma}_{\mathrm{crt}}^*$	0.02	Critical value for deposition
$\phi_{\mathrm{b}}^{\mathrm{f}}$	0.38	Porosity of bottom
α_{E}^*	0.0002	entrainment coefficient
α_{D}^*	0.04	Deposition coefficient
n	0.03	Manning coefficient
Π^{M}	0.04736	Factor for Manning coefficient
$\Delta x = \Delta y$	0.1, 0.2	Mesh size (dimensionless)
CFL	0.1	CFL number

computed results presented in Suzuki et al. (2019) and Tsunetaka et al. (2022). Because the model equations are given in dimensionless form, the first two examples are given and discussed in a nondimensional manner. In the application to the outdoor debris flow experiment, all variables and the employed topographic configurations are converted to dimensional variables to meet the experimental setup.

3.1 Horizontal Flat Plane

In this numerical example, a finite mass of parabolic shape in sectional view is located at a horizontal flat plane. The mass, initially at rest with a solid concentration of 0.5 (i.e., $\phi_0^{\mathrm{s}} = 0.5$), is released and expands radially, forming a deposit heap at the bottom. The initial height of the mass is 1.0, and its base covers a circle with a radius of 3.0. The center of the initial mass sits at the center $(x, y) = (0, 0)$ of the computational domain $[-10, 10] \times [-10, 10]$, and mesh size is $\Delta x = \Delta y = 0.1$. The parameters used in the computation are collected and listed in Table 1.

Figure 3 shows the contours of the evolutions at different time levels, where the results of flow/deposit thickness less than 0.02 are filtered. Those for flow thickness without deposition are given in the panels in row (a), the panels in row (b) are for the flow thicknesses with the depositional process, and the associated deposit heaps are given in the panels in row (c). The corresponding sectional views along $y = 0$ are illustrated in Fig. 4, in which the blue dashed line depicts the heap of deposit and the red line indicates the flow surface. At $t = 2.0$, the deposit heap begins to develop from the center and rapidly grows in the radial direction. At $t = 5.0$, the heap covers nearly the entire bottom area of the flow body. From $t = 10.0$ to 35.0, the heap grows mainly in the vertical direction. At $t = 35.0$, most of the sediments have been deposited, and a very thin flowing layer remains on the top of the heap (cf. Fig. 4b). If no depositional process is considered (panels of Figs. 3a and 4a), the entire flow body comes to a state of

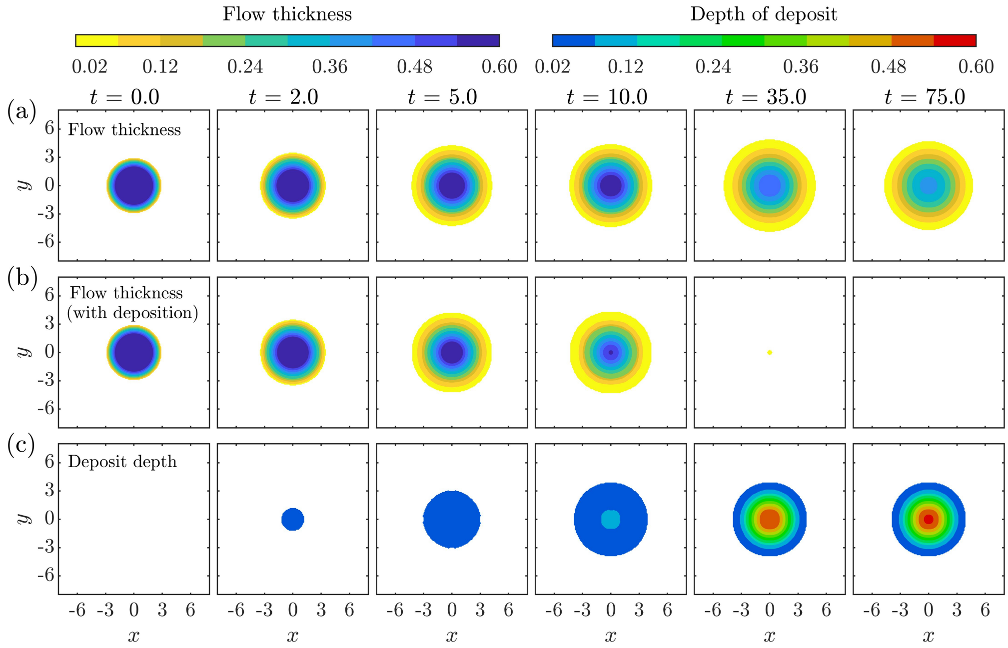

Figure 3. (a) Evolution of the flow body without considering the depositional mechanism; (b) Evolution of the flowing layer (with the depositional mechanism); (c) Evolution of the deposit heap under the flowing layer with respect to panels in (b).

rest at approximately $t = 75.0$ (the maximum speed is less than 0.01 in the computational domain), while the deposit heap has completely developed shortly after $t = 35.0$.

The left panel of Fig. 5 shows a 3D view of the final flow body (at $t = 75.0$), while the right panel displays the final deposit at $t = 35.0$ or 75.0, as shown in Fig. 4b. In addition to the longer duration of mobility, the geometry of the final flow body is much flatter, while the heap of final deposit is more concentrated. These findings reveal that the depositional process significantly impacts both the movement duration and the morphology, for which the deposit heap exhibits a concave shape in the sectional view (cf. Fig. 4b), as elaborated in Chen and Capart (2022).

3.2 Inclined Curved Chute

Besides studying the depositional pattern on the horizontal flat plane, we also examine the depositional process of a flowing finite mass released from an inclined flat plane and merging into a horizontal plane, where a heap of sediment is formed. The chute consists of three sections: the inclined part, the transition section, and the horizontal plane. The computational domain covers $x \in [0, 80]$ in the downslope direction, and $y \in [-18, 18]$ in the transverse direction, where the mesh size is $\Delta x = \Delta y = 0.2$. The inclination angle is $40°$, and the transition section lies in the range $x \in [24, 36]$. The finite mass is released from a parabolic cap with a circular base of radius 3.2 and height 2.0. The center of the cap is located at $(x, y) = (6.0, 0.0)$. The initial solid concentration is 0.5, and the mass is released with a given velocity in the downslope direction. Namely, the x- and y-components of the velocity read

$$v_x(x, y, t = 0) = \begin{cases} 1.2 + (x - 6.0)/3.2 & \text{for} \quad h > 0\,, \\ 0.0 & \text{else}\,, \end{cases} \tag{21}$$
$$v_y(x, y, t = 0) = 0.0\,,$$

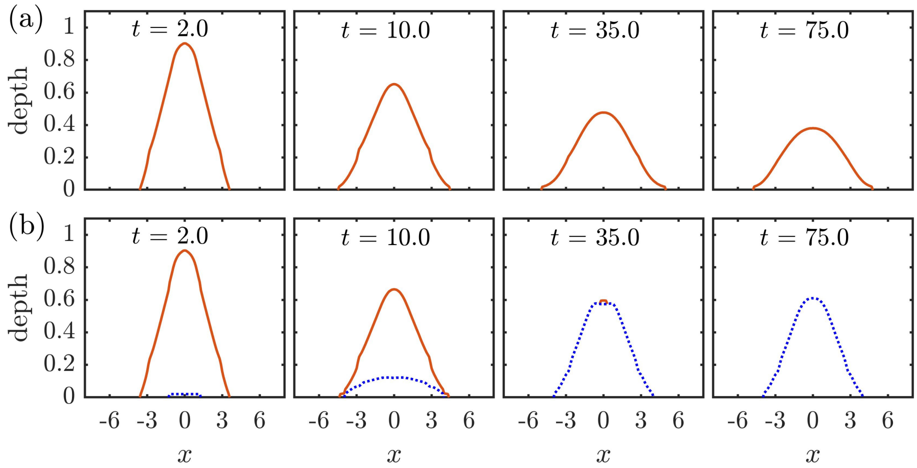

Figure 4. Sectional view (along $y = 0.0$) of the evolutions of the flow surface (red solid line) and deposit heap (blue dotted line). (a) Results computed without the depositional mechanism; (b) Results computed with the depositional mechanism.

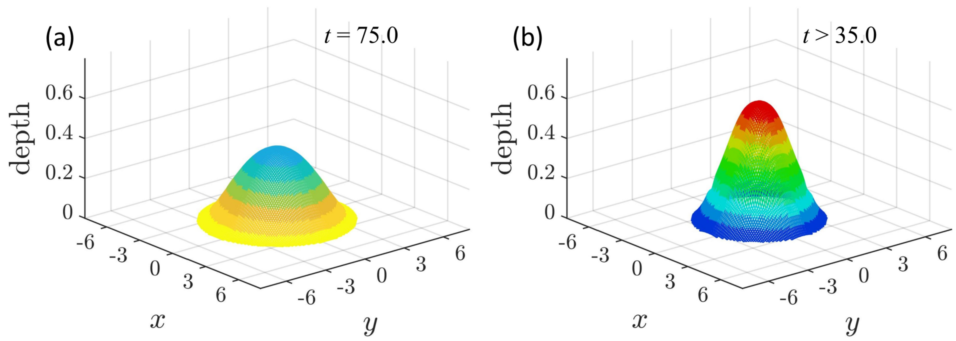

Figure 5. (a) Distribution of the final flow thickness at $t = 75.0$, where no depositional mechanism is considered in the computation; (b) Geometry of the final deposit (cf. the panels of (c) at $t = 35.0$ or 75.0 in Fig. 4).

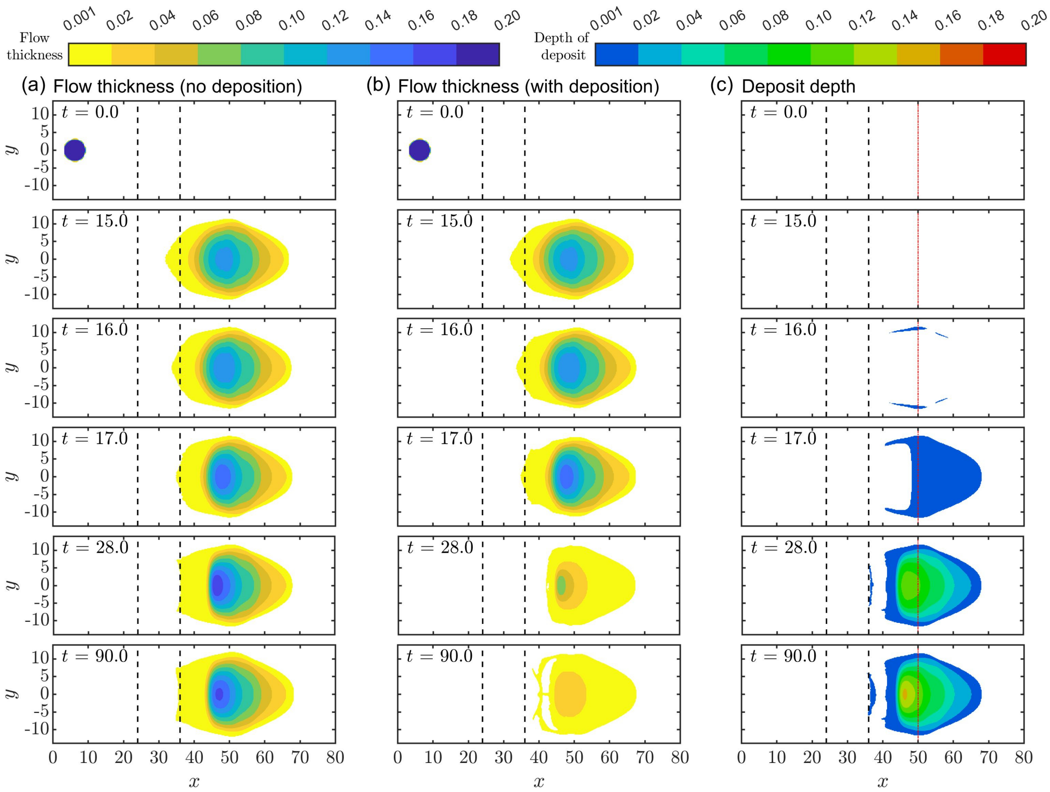

Figure 6. (a) Evolution of the flow body without considering the deposition; (b) Evolution of the flowing layer (with the deposition mechanism); (c) Evolution of the deposit heap under the flowing layer with respect to panels in Column (b). In all panels, the black dashed lines marked the transition section, and the red dash-dotted line indicates the location for the cross-sectional view in Fig. 7.

respectively. The parameters used in the computation are identical to those for the previous example.

Figure 6 illustrates the evolution of the flow body and the associated heap of the deposit by contour plots from $t = 0.0$ to 90.0 at different time levels. The panels in the left column (indexed by a) are the flow thicknesses without considering the process of deposition/entrainment in the computation, the panels in the middle column (indexed by b) present the thickness distributions of the flowing layer where the deposition/entrainment is considered, and the associated heaps of deposits are depicted in the panels in the right column (indexed by c). The black dashed lines mark the transition section, and the red dash-dotted line in Panel c marks the location for the sectional view in Fig. 7b. The corresponding longitudinal sectional views along the chute centerline ($y = 0.0$) are shown in Fig. 7a, while the cross-sectional views at $x = 50.0$ are depicted in Fig. 7b.

Although most of the flow body has passed the transition zone and slowed due to the basal drag at $t = 15.0$, no material deposited because the velocity remained too high. At $t = 16.0$, deposits begin to take place, where heaps of deposits are found on both side flank margins of the tail. The heaps of the deposit develop and extend rapidly, and nearly the entire bottom of the flowing layer of the front half part is covered by a thin heap of deposit (cf. the panels from $t = 16.0$ to 17.0). The levee formation, as presented in Pudasaini et al. (2005); Tai and Kuo (2012) and de Haas et al. (2015), can be observed on both flank margins in the panel at $t = 16.0$ (cf. Fig. 6c and Fig. 7b). Although the

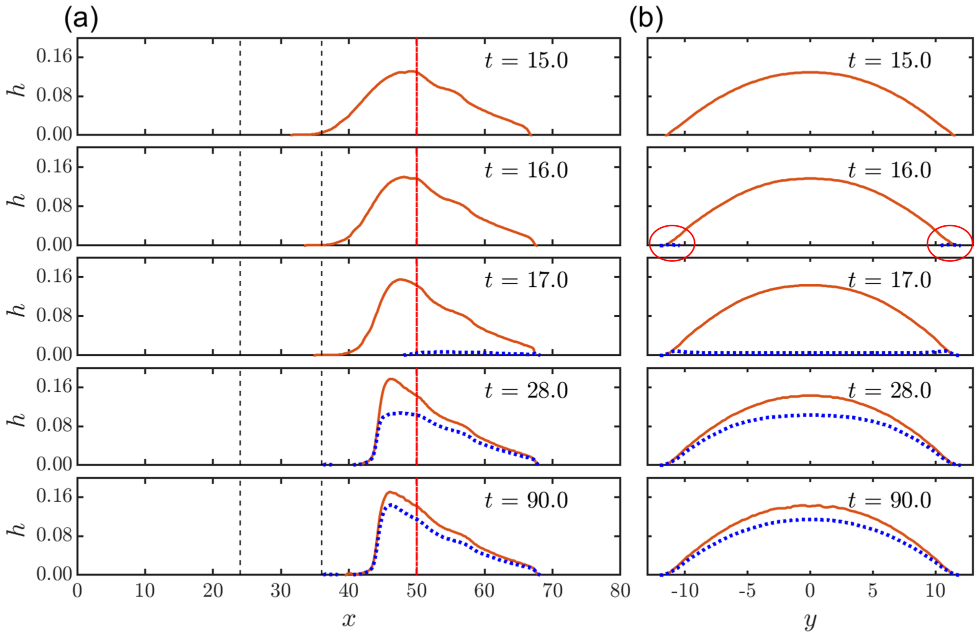

Figure 7. Sectional views of the evolutions of the flow surface (red solid line) and deposit heap (blue dotted line). (a) Sectional view at $y = 0.0$; (b) Sectional view at $x = 50.0$ as indicated by the red dash-dotted line in Panels (a) and in Fig. 6c, where the red circles mark the locations of levees.

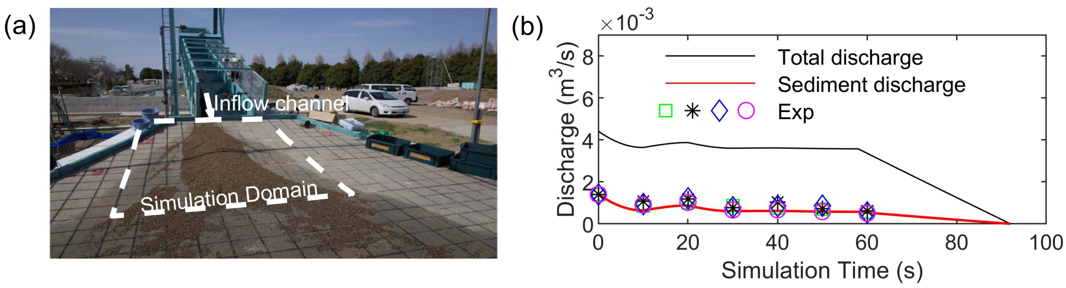

Figure 8. (a) Debris Flow Experiment (modified from Tsunetaka et al. (2019)); (b) The evolution of the discharge into the deposition plane.

levee deposits are not as significant (thick) as shown in Tai and Kuo (2012), the formulae used for the entrainment-deposition rates are totally distinct. From $t = 17.0$ to 28.0, the heap mainly grows in thickness without extending the coverage. At $t = 28.0$, an additional thin heap of deposit develops at the rear, and the main heap of deposit is covered by a thin flowing layer (see Fig. 7). From $t = 28.0$ to 90.0, the rear part of the thin layer slips backward down from the main heap of the deposit due to the high slope. It is interesting to note that the thin layer does not completely deposit because most of the sediments have already been deposited and the remaining concentration is too low for further deposition. At approximately $t = 90.0$, the maximum speed of the flowing layer is less than 0.01 in both cases (with or without considering the process of deposition/entrainment), and it is assumed to be at the state of rest. Moreover, the results here are filtered for flow/deposit thickness values less than 0.001 due to the relatively thin flowing body and deposit.

Table 2. Parameters in computation for simulating the debris flow in experimental in Tsunetaka et al. (2022)

Parameters	Value	Description
$\epsilon = \mathcal{H}/\mathcal{L}$	0.1 m/0.1 m	Aspect Ratio
$\alpha_\rho = \rho^{\mathrm{f}}/\rho^{\mathrm{s}}$	0.37879	Density Ratio (1.00/2.64)
x	$\in$[0, 6] m	Domain in x-direction
y	$\in$[-2.2,2.2] m	Domain in y-direction
$\Delta x = \Delta y$	0.02 m	Mesh size
δ_{b}	34.2°	Angle of basal friction (solid)
$\vartheta^{\mathrm{f}}_{\mathrm{b}}$	0.1	Navier fluid friction coefficient
c_{d0}	1.5	Drag coefficient
μ^{f}	1.0526 mPa·s	Viscosity of interstitial fluid
N_R	94,048	Viscous number
d	0.0026 m	Sediment median diameter
$\tilde{\Psi}^*_{\mathrm{crt}}$	0.04	Critical Shields parameter
$\tilde{\mathrm{v}}$	1.6	Dimensionless critical speed for deposition
$\tilde{\Sigma}^*_{\mathrm{crt}}$	0.016	Critical value for deposition
$\phi^{\mathrm{f}}_{\mathrm{b}}$	0.38	Porosity of bottom
α^*_{E}	0.00008	Entrainment coefficient
α^*_{D}	0.04	Deposition coefficient
n	0.016	Manning coefficient
Π^{M}	0.04736	Factor for Manning coefficient
CFL	0.1	CFL number

3.3 Application to Debris Flow Experiment

The proposed model is applied to the debris flow experiment in Suzuki et al. (2019) and Tsunetaka et al. (2022) for validation. In the experiment, a water-sediment mixture is released from a straight flume channel, which is 8.0 m long, 0.1 m wide and inclined with an angle of 15°. As shown in Fig. 8a, the channel is connected to a flat plane, which serves as the deposition zone. The inclination angle of this plane decreases at a rate of 3° per meter in the longitudinal direction from 12° to 3°. The investigation focuses on the flat deposition zone, such that a computational domain $[0.0, 6.0]\times[-2.2, 2.2]$ (in m) is assigned, cf. Fig. 8a. The debris flow enters the computational domain from the flume channel at $x = 0.0$. The inflow condition is set based on the experimental data (cf. Suzuki et al., 2019; Tsunetaka et al., 2022), such that a uniform depth of 20 cm sediment of a median diameter $d = 2.6$ mm on the flume bed was flushed and allowed to flow into the computational domain by a water supply of 3×10^{-3} m^3/s at the top of the flume for a duration of 60 s. Figure 8b illustrates the inflow condition in the computation, in which the total (water and sediment) discharge is depicted by the blue solid line, and the red line indicates sediment discharge. The sediment discharge is set by the mean value of four separate runs, whereas Suzuki et al. (2019) reported sediment concentrations of approximately 32% when the debris front reached the end of the flume, and ca. 16% at the end of the water supply (i.e., at $t = 60$ s). In the computation, the inflow vanishes at $t = 92$ s, and the simulation ends at $t = 100$ s. We refer the readers to Appendix A for details on the inflow condition used in the computation.

In the experiments, sediment particles (ca. 1 mm in diameter) were glued on the surface of the deposition zone to represent the roughness. Consequently, the Manning coefficient is set to 0.016 (cf. Chow, 1959) in the computation. The grain-water mixture consisted of water and quasi-mono-dispersed sediment particles, whose grain size ranges

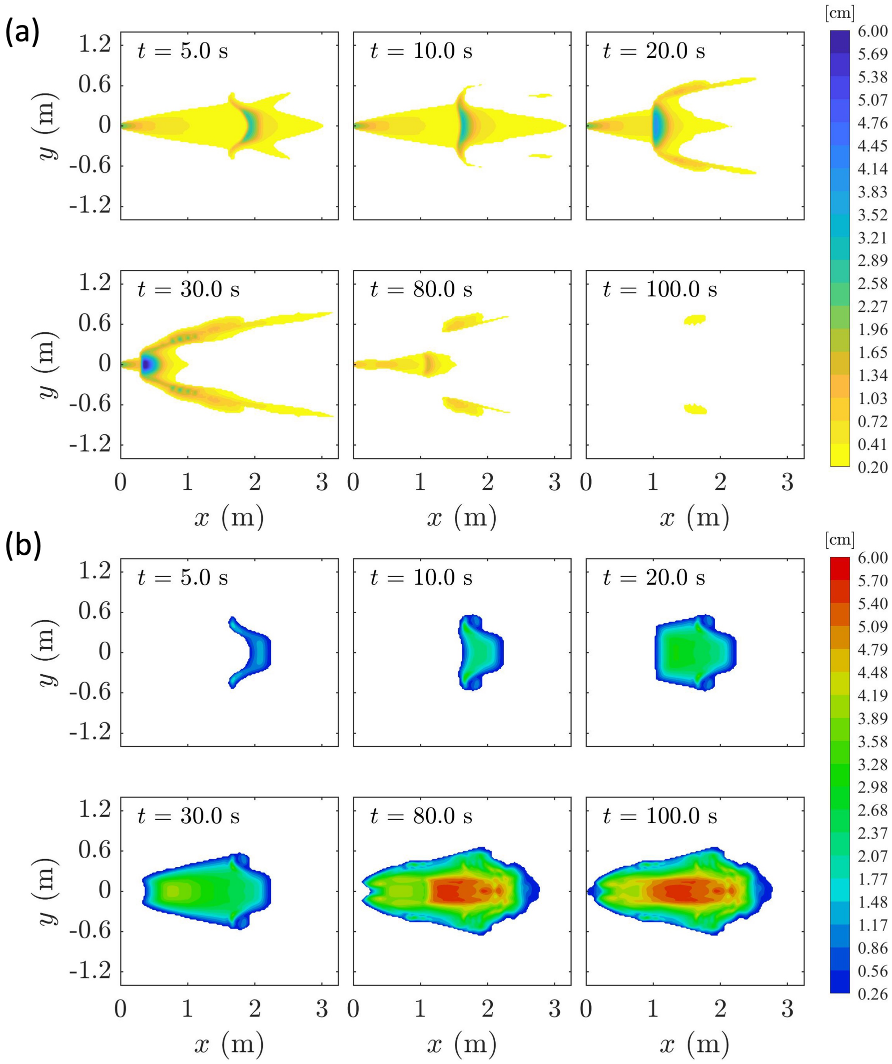

Figure 9. (a) Thickness distribution of the simulated flowing layer. (b) Evolution of the deposit heap in the computation.

from 2.02 to 3.24 mm, with a mean size $D_{50} = 2.6$ mm. Hence, we choose $\tilde{\Psi}_{\rm crt} = 0.04$ as the critical Shields value for entrainment in the computation. For the deposit, we set the critical value to $\tilde{\Sigma}_{\rm crt} = 0.016$ in (14) and the dimensionless critical speed to $\tilde{\rm v} = 1.6$, which is equivalent to 0.2554 m/s for a sediment grain size of 2.6 mm. In the Hjulström-Sundborg diagram (Hjulström, 1935), this value lies in the transition band between erosion and deposition. According to Tsunetaka et al. (2022), the sediment particles have a density is $2,640$ kg/m^3, and an angle of internal friction of approximately 34°, which was used as 34.2° in the simulation. For a concise overview, all simulation parameters used in the computation are collected and listed in Table 2.

Figure 9a demonstrates the distributions of flow thickness at different time levels, where the associated deposits are given in Fig. 9b. At $t = 5.0$ s, a sharp change of flow thickness (similar to the hydraulic jump) is found at approximately $x = 1.9$ m, which moves backwards to ca. $x = 1.0$ m at $t = 20.0$ s and $x = 0.5$ m at $t = 30.0$ s. This migration of the hydraulic jump develops together with the migration of the heap of deposit (cf. Fig. 9b). This finding indicates that the flow behavior is highly related to the

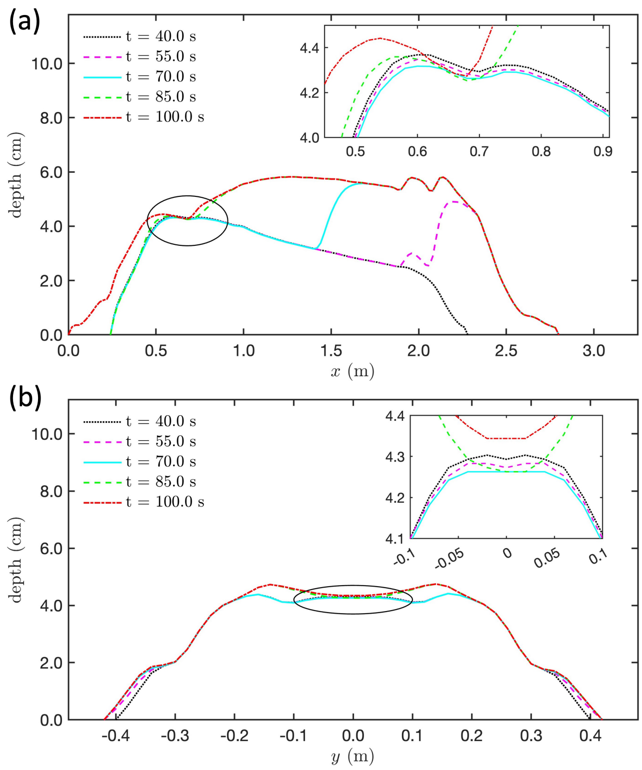

Figure 10. Evolution of the deposit pile, where the inlet plots show the local view of area marked with a black line. (a) Longitudinal sectional view at $y = 0.0$; and (b) transverse sectional view at $x = 0.7$ m (cf. Fig. 9b).

development of the heap deposit. When the deposit heap first develops, it is in a concave shape with the opening facing the stream ($t = 5.0$ s). The notch is filled as time increases ($t = 5.0$ s to 10.0 s). From $t = 10.0$ to 30.0 s, the heap mainly grows along the stream direction. At approximately $t = 80.0$ s, the area of the heap has reached the final shape, and the thickness increases significantly from $t = 80.0$ to 100.0 s. Either the moving mass has flowed out from the computational domain or the thickness of most flowing layer is less than 0.2 cm at $t = 100.0$ s, when the deposit heap has reached the final geometry. Exploring the flow behaviors and the development of the deposit heap shows that the jump patterns of the flow correspond to the fronts of the deposit heap developing at the bottom.

Another interesting finding is that the propagating front of the deposit heap is correlated with the layered deposition. Figure 10 shows the longitudinal (at $y = 0.0$ m) and transverse (at $x = 0.7$ m) sectional views of the evolving deposit heap at various time levels. At around $t = 40.0$ s, the bottom layer of the deposit had fully developed, while the flow flux remained high and continued from above. As a result, the flowing material overrode the existing deposit pile and deposited both behind and on top of it ($t = 55.0$ s in Fig. 10a). Between $t = 55.0$ s and 85.0 s, material continued to deposit on the top of the existing heap, so that a new pile grew as a traveling wave propagating upstreams on top of the previously deposited heap. This process resulted in a layered formation of the deposit (cf. Fig. 10a). While the deposit dominates the overall process, some entrainment (erosion) can still be observed in certain locations. As shown in the inlet plots in Fig. 10ab, which provide sectional views at $y = 0.0$ m and $x = 0.7$ m, respectively, erosion can be identified during the time interval $t \in [40.0, 70.0]$ s, followed by depo-

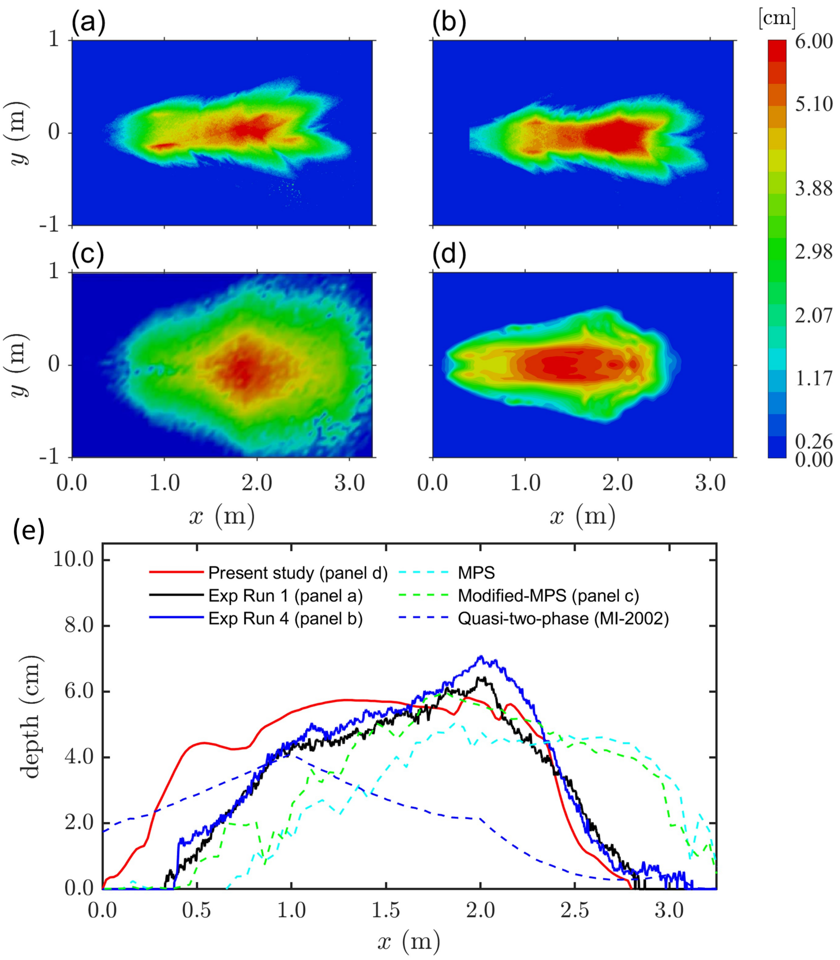

Figure 11. Top view of the final deposits, where (a) measurement in experiment (run1), (b) measurement in experiment (run4) (c) result computed by modified MPS in Suzuki et al. (2019), and (d) results computed by the present proposed model. (e) Longitudinal sectional views (along $y = 0.0$ m) of the various computed results and experimental measurements. (Panels (a) and (b) are extracted from Tsunetaka et al. (2022), Panel (c) is from Suzuki et al. (2019), and Panel (e) is modified based on Suzuki et al. (2019).)

sition from $t = 70.0$ s to 100.0 s. It is remarkable that the transverse sectional view of the deposit heap exhibits a translation from a flat plane to a concave shape between $t =$ 70.0 s and 100.0 s. This concave shape can also be regarded as a prototype for the formation of levees.

In addition to the development process of the deposit, we also examine the final geometry of the deposit heap computed by different models and the experimental deposit heaps. The comparison includes the results illustrated in Suzuki et al. (2019), in which a Modified-MPS approach and a quasi-two-phase model (Miyamoto & Itoh, 2002) were employed. Figure 11abcd shows the top views of the final deposit. Panels (a) and (b) illustrate the measurements in experiments with mono-granular particles, where the data are extracted from Runs 1 and 4, as listed in Tsunetaka et al. (2022). Panel (c) presents the results computed by a Modified-MPS approach (see Suzuki et al., 2019), and Panel (d) shows the results given in the panel of $t = 100.0$ s in Fig. 9b which is regarded as the final geometry of the deposit heap computed by the proposed model. Because the deposit computed by a quasi-two-phase model (Miyamoto & Itoh, 2002) is significantly worse than those computed by other models (cf. Fig. 11e), it is not considered in the present discussion. The Modified-MPS approach delivered a deposit (Panel c) that is in oval shape and features a single peak lying approximately at the center. In contrast, the deposit (Panel d) computed by the proposed model exhibits a long strip with multiple deposit peaks. Although the computed deposit covers a slightly larger area, the location of the high peaks mimics the locations measured in experiments.

The longitudinal sectional views of the final deposits are depicted in Fig 11e, in which the red solid line indicates the deposit computed by the present model, and the black and blue solid lines present the measurements in the mono-granular tests, the green and cyan dotted lines respectively are the results computed by the MPS and Modified MPS methods given in Suzuki et al. (2019), and the blue dashed line represents the results by the quasi-two-phase model (Miyamoto & Itoh, 2002, denoted by MI-2002). Although the MPS and Modified MPS methods can capture the peak at around $x = 1.9$ m, the present study (red solid line) also delivers sound agreement. Together with the feature of multiple peaks for the deposit heap, the present two-phase model can more appropriately describe the debris flows with deposition.

4 Concluding remarks

We presented a new two-phase fluid-grain model with entrainment and deposition for debris flows on rugged topographic surfaces, where the basal shear stress determines the entrainment and the sediment settling process yields deposition. The model equations are derived with respect to a terrain-following coordinate system as employed in Tai et al. (2012); Tai and Kuo (2012); Luca et al. (2016) or Tai et al. (2019). Unlike the deformation coordinates used in Tai et al. (2012) or Tai and Kuo (2012), the heaps of deposit or the potholes of erosion are described by adding a ”subtopography” over the topographic surface, i.e., as a deviation from the initial topography before entrainment/deposition. In addition, the entrainment-deposition mechanism is implemented and integrated into a CUDA-GPU-accelerated simulation tool (Ko et al., 2021) for high-performance computation.

This proposed model was investigated with two idealized numerical examples and one validation against experimental measurements. The example on the horizontal plane showed that the duration of movement is much longer if no depositional process is considered because the material cannot arrive at the state of rest. Not only is this phenomenon related to the duration of movement, but the final geometry of the deposit heap also differs from the one computed based on the depositional mechanism. This finding emphasizes one of the key impacts of the depositional process on the associated flow behaviors and on the local morphology after a debris flow event. Remarkably, levee formation is observed in the example of chute topography, where a finite mass is released from the top of the inclined section and deposits on the horizontal plane. The simulation of the debris flow experiment not only reproduces the formation of levees but also exposes a layered pattern of deposits. This layered deposition indicates that a stratified pattern can form within a single debris flow event and provides insight into one of the causes for the stratified scree deposits (e.g., Sass & Krautblatter, 2007; Van Steijn, 2011; de Haas et al., 2018). While there were some discrepancies in simulating the debris flow experiments, the computed deposit heap ended up in roughly the same position as the experimental deposit heap. Furthermore, the computed heap featured multiple peaks (such as the concave shape in transverse sectional view), just like those observed in the long strip deposit heap.

Although the results have shown the key features of the present two-phase erodible model and shed light on simulating the entrainment-deposition process, this model is still limited by the idealized conditions given in the three examples. For example, in addition to the complex rheology of debris flows, the in situ entrainment-deposition processes are highly related to the material composition and the local geological conditions. The complex material composition and heterogeneous conditions lead to a tremendous challenge in modeling. Although reasonable or strong assumptions have been imposed to simply the model equations, the degree of uncertainty in the associated parameter calibration remains extremely high. The present model is a compromised approach, but its numerical implementation is uncomplicated. For the sake of engineering applications, we can make good use of the GPU-accelerated facility for highly efficient computation. That is, simulations can help to investigate and evaluate plausible scenarios using abundant parameter sets, and can typically be performed and completed within a few hours or days, depending on the number of scenarios and the complexity of the parameter sets. With these advantages, engineering applications of the present model for hazard assessment or evaluation of plausible disasters mitigation countermeasures can be expected.

Appendix A Inflow condition in the computation for the debris flow experiment

The inflow condition is set in two stages. A constant inflow rate of $Q_{\text{in}}^{I} = 3\times10^{-3}$ m^3/s is maintained for $t \in [0.0, 58.0]$ s, while Q_{in}^{II} linearly reduces to zero from $t = 58.0$ s to $t = 92.0$ s. More precisely,

$$Q_{\text{in}}(t) = \begin{cases} Q_{\text{in}}^{I}(t) = Q_{\text{supply}} & \text{for} \quad t \in [\,0.0, 58.0]\ \text{s}, \\ Q_{\text{in}}^{II}(t) = Q_{\text{supply}}\,(92 - t)/34 & \text{for} \quad t \in [58.0, 92.0]\ \text{s}, \end{cases} \tag{A1}$$

where $Q_{\text{supply}} = 3 \times 10^{-3}$ m^3/s. The sediment concentration is set according to the measurements given in Suzuki et al. (2019) using

$$\phi^{\text{s}}(t) = \begin{cases} \phi_a^{\text{s}} - (\phi_a^{\text{s}} - \phi_b^{\text{s}})\ \cos\left(\dfrac{t_b - t}{t_b - t_a}\right) & \text{for} \quad t \in [\,0.0, 58.0]\ \text{s}, \\ \phi_a^{\text{s}} - (\phi_a^{\text{s}} - \phi_b^{\text{s}})\left[1.0 - \dfrac{(t_b - t)}{(t_b - t_a)}\right] & \text{for} \quad t \in [58.0, 92.0]\ \text{s} \end{cases} \tag{A2}$$

with the values of t_a, t_b, ϕ_a^{s} and ϕ_b^{s} listed in Table A1.

Similar to the inflow rate, the inflow height is initially set to 0.022 m for $t \in [0.0, 58]$ s, and then it linearly decreases to zero over the period of $[58.0, 92.0]$ s. That is,

$$h_{\text{in}}^{\text{T}}(t) = \begin{cases} 0.022 & \text{for} \quad t \in [\,0.0, 58.0]\ \text{s}, \\ 0.022 \times (92 - t)/34 & \text{for} \quad t \in [58.0, 92.0]\ \text{s}\,. \end{cases} \tag{A3}$$

As a result, the depths of the sediment and fluid phases in the inflow condition are given by

$$h_{\text{in}}^{\text{s}}(t) = h_{\text{in}}^{\text{T}}(t)\,\phi^{\text{s}}(t) \quad \text{and} \quad h_{\text{in}}^{\text{f}}(t) = h_{\text{in}}^{\text{T}}(t) - h_{\text{in}}^{\text{s}}(t), \tag{A4}$$

respectively. The inflow velocity is assumed to be uniformly distributed with zero relative velocity between the phases. With (A1), (A4), and the flume width $B_{\text{flume}} = 0.1$ m, the inflow velocity remains constant and is given by

$$\begin{cases} v_{x,\text{in}}^{\text{s}} = v_{x,\text{in}}^{\text{f}} = \dfrac{Q_{\text{in}}(t)}{h_{\text{in}}^{\text{T}}(t)\,B_{\text{flume}}} = 1.364\ \text{m/s}\,, \\ v_{y,\text{in}}^{\text{s}} = v_{y,\text{in}}^{\text{f}} = 0.0\ \text{m/s}\,. \end{cases} \tag{A5}$$

Open Research Section

The data and code for reproducing the results shown in the present manuscript are available at https://doi.org/10.6084/m9.figshare.21893943.v4.

Table A1. Parameters for computing the inflow condition

time period (s)	ϕ_a^s	ϕ_b^s	t_a	t_b
$[0.0, 5.0]$	0.32	0.175	0.0	5.0
$[5.0, 20.0]$	0.175	0.225	5.0	20.0
$[20.0, 30.0]$	0.225	0.167	20.0	30.0
$[30.0, 40.0]$	0.167	0.17	30.0	40.0
$[40.0, 58.0]$	0.17	0.16	40.0	58.0
$[58.0, 92.0]$	0.16	0.15	58.0	92.0

Acknowledgments

This study was initiated by the MOST add-on Grant for International Cooperation between Japan and Taiwan in 2020. H.K. Wong and Y.C. Tai acknowledge the warm hospitality of the Japanese partners at UTokyo, CTI, PWRI and UTsukuba. In addition, the financial support of the Ministry of Science and Technology, Taiwan (MOST 109-2221-E-006-022-) and the Soil and Water Conservation Bureau, Council of Agriculture, Taiwan (SWCB-111-035) are sincerely acknowledged.

References

Berenbrock, C., & Tranmer, A. W. (2008). *Simulation of flow, sediment transport, and sediment mobility of the lower coeur d'alene river, idaho* (Vol. 5093). US Geological Survey Reston, VA.

Berger, C., McArdell, B. W., Fritschi, B., & Schlunegger, F. (2010). A novel method for measuring the timing of bed erosion during debris flows and floods. *Water Resources Research*, *46*(2).

Bouchut, F., Fernández-Nieto, E. D., Koné, E. H., Mangeney, A., & Narbona-Reina, G. (2017). A two-phase solid-fluid model for dense granular flows including dilatancy effects: comparison with submarine granular collapse experiments. In *Epj web of conferences* (Vol. 140, p. 09039).

Bouchut, F., Fernández Nieto, E. D., Mangeney, A., & Narbona Reina, G. (2016). A two-phase two-layer model for fluidized granular flows with dilatancy effects. *Journal of Fluid Mechanics, 801, 166-221.*.

Bouchut, F., & Westdickenberg, M. (2004). Gravity driven shallow water models for arbitrary topography. *Comm. Math. Sci*, *2*, 359-389.

Cao, Z., Pender, G., Wallis, S., & Carling, P. (2004). Computational dam-break hydraulics over erodible sediment bed. *Journal of hydraulic engineering*, *130*(7), 689–703.

Chen, H., Crosta, G. B., & Lee, C. F. (2006). Erosional effects on runout of fast landslides, debris flows and avalanches: a numerical investigation. *Geotechnique*, *56*(5), 305–322.

Chen, H., Zhang, L. M., Chang, D. S., & Zhang, S. (2012). Mechanisms and runout characteristics of the rainfall-triggered debris flow in Xiaojiagou in Sichuan Province, China. *Natural Hazards*, *62*(3), 1037–1057.

Chen, H., Zhang, L. M., & Zhang, S. (2014). Evolution of debris flow properties and physical interactions in debris-flow mixtures in the Wenchuan earthquake zone. *Engineering Geology*, *182*, 136–147.

Chen, T., & Capart, H. (2022). Computational morphology of debris and alluvial fans on irregular terrain using the visibility polygon. *Computers & Geosciences*, 105228.

Chow, V.-T. (1959). *Open-channel hydraulics.* McGraw-Hill, New York.

de Haas, T., Braat, L., Leuven, J. R., Lokhorst, I. R., & Kleinhans, M. G. (2015). Effects of debris flow composition on runout, depositional mechanisms, and deposit morphology in laboratory experiments. *Journal of Geophysical Research: Earth Surface*, *120*(9), 1949–1972.

de Haas, T., Densmore, A., Stoffel, M., Suwa, H., Imaizumi, F., Ballesteros-Cánovas, J., & Wasklewicz, T. (2018). Avulsions and the spatio-temporal evolution of debris-flow fans. *Earth-Science Reviews*, *177*, 53–75.

Earle, S. (2015). *Physical geology.* BCcampus.

Egashira, S. (1997). Constitutive equations of debris flow and their applicability. In *1st. international conference on debris-flow hazards mitigation, asce, 1997* (pp. 340–349).

Fraccarollo, L., & Capart, H. (2002). Riemann wave description of erosional dam-break flows. *Journal of Fluid Mechanics*, *461*, 183–228.

Heß, J., Tai, Y.-C., & Wang, Y. (2019). Debris flows with pore pressure and intergranular friction on rugged topography. *Computers & Fluids*, *190*, 139–155.

Hjulström, F. (1935). *Studies of the morphological activity of rivers as illustrated by the river fyris* (Unpublished doctoral dissertation). The Geological institution of the University of Upsala.

Hungr, O., McDougall, S., & Bovis, M. (2005). Entrainment of material by debris flows. In *Debris-flow hazards and related phenomena* (pp. 135–158). Springer.

Hutter, K., Svendsen, B., & Rickenmann, D. (1996). Debris flow modeling: A review. *Continuum mechanics and thermodynamics*, *8*(1), 1–35.

Issler, D. (2014). Dynamically consistent entrainment laws for depth-averaged avalanche models. *Journal of fluid mechanics*, *759*, 701–738.

Iverson, R. M. (2012). Elementary theory of bed-sediment entrainment by debris flows and avalanches. *Journal of Geophysical Research: Earth Surface*, *117*(F3).

Iverson, R. M., & George, D. L. (2014). A depth-averaged debris-flow model that includes the effects of evolving dilatancy. I. physical basis. *Proceedings of the Royal Society A: Mathematical, Physical and Engineering Sciences*, *470*(2170), 20130819.

Ko, C.-J., Chen, P.-C., Wong, H.-K., & Tai, Y.-C. (2021). MoSES_2PDF: A GIS-compatible GPU-accelerated high-performance simulation tool for grain-fluid shallow flows. *arXiv preprint arXiv:2104.06784*.

Kurganov, A., & Petrova, G. (2007). A second-order well-balanced positivity preserving central-upwind scheme for the saint-venant system. *Communications in Mathematical Sciences*, *5*(1), 133–160.

Kurganov, A., & Tadmor, E. (2000). New high-resolution central schemes for nonlinear conservation laws and convection–diffusion equations. *Journal of Computational Physics*, *160*(1), 241–282.

Li, S., & Duffy, C. J. (2011). Fully coupled approach to modeling shallow water flow, sediment transport, and bed evolution in rivers. *Water Resources Research*, *47*(3).

Luca, I., Kuo, C.-Y., Hutter, K., & Tai, Y.-C. (2012). Modeling shallow over-saturated mixtures on arbitrary rigid topography. *Journal of Mechanics*, *28*(3), 523–541.

Luca, I., Tai, Y.-C., & Kuo, C.-Y. (2009). Non-cartesian, topography-based avalanche equations and approximations of gravity driven flows of ideal and viscous fluids. *Mathematical Models and Methods in Applied Sciences*, *19*(01), 127–171.

Luca, I., Tai, Y.-C., & Kuo, C.-Y. (2016). *Shallow geophysical mass flows down arbitrary topography.* Springer-Verlag.

Ma, C.-Y., Ko, C.-J., Wong, H.-K., & Tai, Y.-C. (2022). Modeling three-phase debris flows in terrain-following coordinate system and its GPU computation with CUDA structure. *Journal of the Chinese Institute of Civil and Hydraulic Engineering*, *34*(7), 597–604 (in Chinese).

Meng, X., & Wang, Y. (2016). Modelling and numerical simulation of two-phase debris flows. *Acta Geotechnica*, *11*(5), 1027–1045.

Miyamoto, K., & Itoh, T. (2002). Numerical simulation method of debris flow introducing the erosion rate equation. *Journal of the Japan society of erosion control engineering*, *55*(2), 24–35.

Nishiguchi, Y., & Uchida, T. (2022). Long-runout-landslide-induced debris flow: The role of fine sediment deposition processes in debris flow propagation. *Journal of Geophysical Research: Earth Surface*, *127*(2), e2021JF006452.

Pierson, T. C., Janda, R. J., Thouret, J.-C., & Borrero, C. A. (1990). Perturbation and melting of snow and ice by the 13 november 1985 eruption of nevado del ruiz, colombia, and consequent mobilization, flow and deposition of lahars. *Journal of Volcanology and Geothermal Research*, *41*(1-4), 17–66.

Pitman, E., & Le, L. (2005). A two-fluid model for avalanche and debris flows. *Philosophical Transactions of the Royal Society A: Mathematical, Physical and Engineering Sciences*, *363*(1832), 1573–1601.

Pitman, E., Nichita, C., Patra, A., Bauer, A., Bursik, M., & Webb, A. (2003). A model of granular flows over an erodible surface. *Discrete & Continuous Dynamical Systems-B*, *3*(4), 589.

Pudasaini, S. P. (2012). A general two-phase debris flow model. *Journal of Geophysical Research: Earth Surface*, *117*(F3).

Pudasaini, S. P., & Fischer, J.-T. (2020). A mechanical erosion model for two-phase mass flows. *International Journal of Multiphase Flow*, *132*, 103416.

Pudasaini, S. P., & Mergili, M. (2019). A multi-phase mass flow model. *Journal of Geophysical Research: Earth Surface*, *124*(12), 2920–2942.

Pudasaini, S. P., Wang, Y., & Hutter, K. (2005). Modelling debris flows down general channels. *Natural Hazards and Earth System Sciences*, *5*(6), 799–819.

Sarno, L., Carravetta, A., Tai, Y.-C., Martino, R., Papa, M., & Kuo, C.-Y. (2018). Measuring the velocity fields of granular flows–employment of a multi-pass two-dimensional particle image velocimetry (2d-piv) approach. *Advanced Powder Technology*, *29*(12), 3107–3123.

Sass, O., & Krautblatter, M. (2007). Debris flow-dominated and rockfall-dominated talus slopes: Genetic models derived from GPR measurements. *Geomorphology*, *86*(1-2), 176–192.

Shields, A. (1936). *Application of similarity principles and turbulence research to bed-load movement.* California Institute of Technology.

Shirsath, S., Padding, J., Clercx, H., & Kuipers, J. (2015). Cross-validation of 3D particle tracking velocimetry for the study of granular flows down rotating chutes. *Chemical engineering science*, *134*, 312–323.

Suzuki, T., & Hotta, N. (2016). Development of modified particles method for simulation of debris flow using constitutive equations. *International Journal of Erosion Control Engineering*, *9*(4), 165–173.

Suzuki, T., Hotta, N., & Miyamoto, K. (2009). Numerical simulation method of debris flow introducing the non-entrainment erosion rate equation, at the transition point of riverbed gradient or the channel width and in the area of sabo dam. *Journal of the Japan Society of Erosion Control Engineering*, *62*(3), 14–22.

Suzuki, T., Hotta, N., Tsunetaka, H., & Sakai, Y. (2019). Application of an MPS-based model to the process of debris-flow deposition on alluvial fans. *Association of Environmental and Engineering Geologists; special publication 28*.

Tai, Y.-C., Heß, J., & Wang, Y. (2019). Modeling two-phase debris flows with grain-fluid separation over rugged topography: Application to the 2009 Hsiaolin event, Taiwan. *Journal of Geophysical Research: Earth Surface*, *124*(2), 305–333.

Tai, Y.-C., & Kuo, C.-Y. (2008). A new model of granular flows over general topography with erosion and deposition. *Acta Mechanica*, *199*(1-4), 71–96.

Tai, Y.-C., & Kuo, C.-Y. (2012). Modelling shallow debris flows of the Coulomb-mixture type over temporally varying topography. *Natural Hazards and Earth System Sciences*, *12*(2), 269–280.

Tai, Y.-C., Kuo, C.-Y., & Hui, W.-H. (2012). An alternative depth-integrated formulation for granular avalanches over temporally varying topography with small curvature. *Geophysical & Astrophysical Fluid Dynamics*, *106*(6), 596–629.

Takahashi, T. (2007). *Debris flow: mechanics, prediction and countermeasures.* Taylor & Francis.

Takahashi, T., Nakagawa, H., Harada, T., & Yamashiki, Y. (1992). Routing debris flows with particle segregation. *Journal of Hydraulic Engineering*, *118*(11), 1490–1507.

Tsunetaka, H., Hotta, N., Sakai, Y., Nishighchi, Y., & Hina, J. (2019). Experimental examination for influence of debris-flow hydrograph on development processes of debris-flow fan. *Association of Environmental and Engineering Geologists; special publication 28*.

Tsunetaka, H., Hotta, N., Sakai, Y., & Wasklewicz, T. (2022). Effect of debris-flow sediment grain-size distribution on fan morphology. *Earth Surface Dynamics*, *10*(4), 775–796.

Van Steijn, H. (2011). Stratified slope deposits: periglacial and other processes involved. *Geological Society, London, Special Publications*, *354*(1), 213–226.

Zhang, R. (1989). *Sediment dynamics in rivers.* Hydraulic and Water Power Press of China, Beijing.

Figure 2.

Flow thickness
0.02
0.12
0.24
0.36
0.48
0.60
Depth of deposit
0.02
0.12
0.24
0.36
0.48
0.60
$t = 0.0$
$t = 2.0$
$t = 5.0$
$t = 10.0$
$t = 35.0$
$t = 75.0$
(a)
Flow thickness
(b)
Flow thickness
(with deposition)
(c)
Deposit depth
6
3
0
-3
-6
y
x

Figure 02.

Entrainment
Deposition
v^*
ϕ^{S}
$\mathcal{E}^{\mathrm{S}*}$
$\times 10^{-3}$
0
0.1
0.2
0.3
0.4
0.5
0.6
0.7
2
-2
-4
-6
-8

Figure 3.

(a)
(b)
depth
depth
t = 2.0
t = 10.0
t = 35.0
t = 75.0
t = 2.0
t = 10.0
t = 35.0
t = 75.0
0
0.2
0.4
0.6
0.8
1
-6
-3
0
3
6
x

Figure 05.


(a)
t = 75.0
depth
0.6
0.4
0.2
0
-6
-3
0
3
6
x
-6
-3
0
3
6
y
(b)
t > 35.0
depth
0.6
0.4
0.2
0
-6
-3
0
3
6
x
-6
-3
0
3
6
y

Figure 5.


Flow thickness
0.001 0.02 0.04 0.06 0.08 0.10 0.12 0.14 0.16 0.18 0.20
Depth of deposit
0.001 0.02 0.04 0.06 0.08 0.10 0.12 0.14 0.16 0.18 0.20
(a) Flow thickness (no deposition)
(b) Flow thickness (with deposition)
(c) Deposit depth
$t = 0.0$
$t = 15.0$
$t = 16.0$
$t = 17.0$
$t = 28.0$
$t = 90.0$
y
x

Figure 07.

(a)
(b)
t = 15.0
t = 16.0
t = 17.0
t = 28.0
t = 90.0
h
0.16
0.08
0.00
0
10
20
30
40
50
60
70
80
x
-10
-5
0
5
10
y

Figure 7.


(a)
Inflow channel
Simulation Domain
(b)
×10^-3
Discharge (m^3/s)
8
6
4
2
0
0
20
40
60
80
100
Simulation Time (s)
Total discharge
Sediment discharge
Exp

Figure 09.

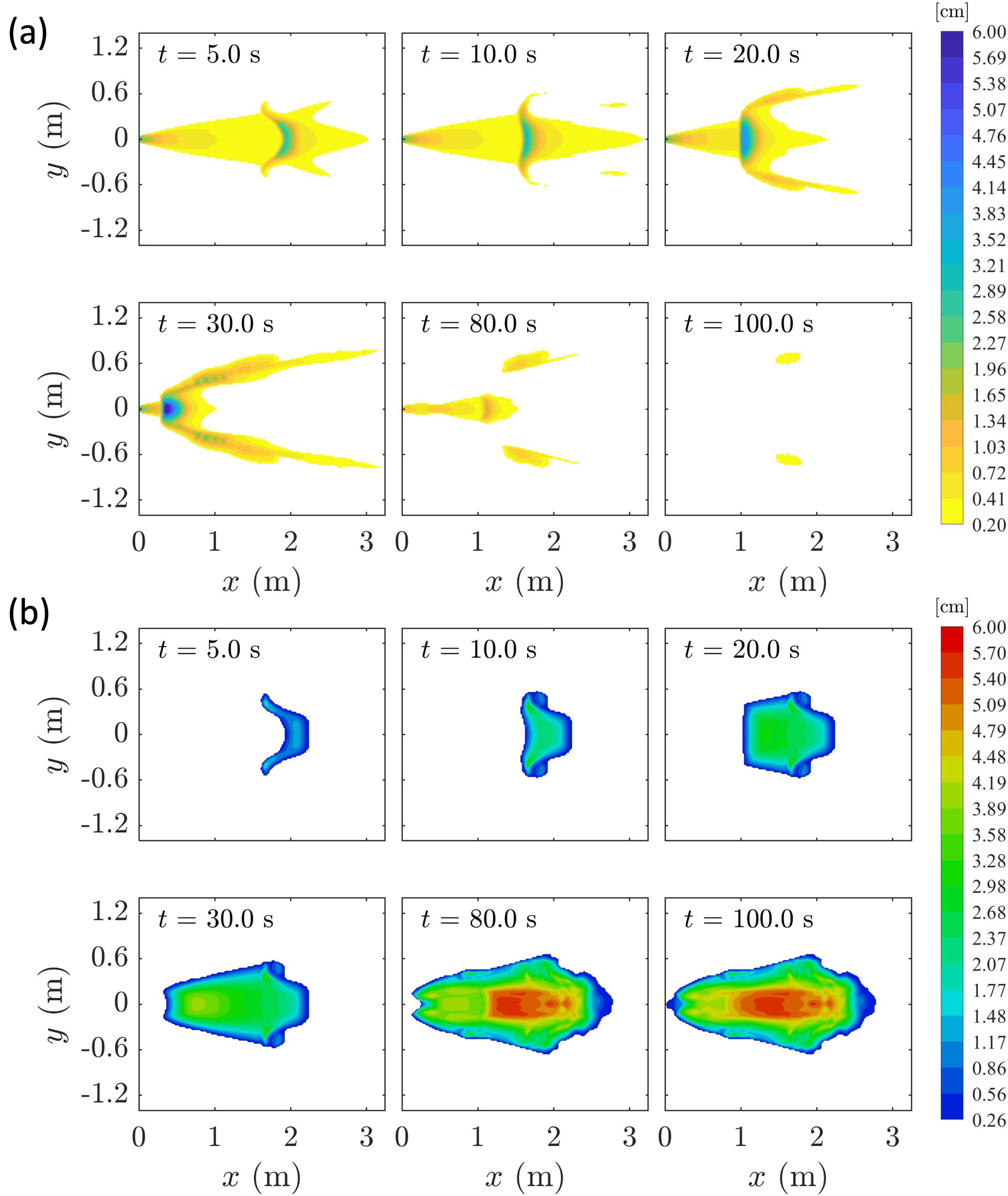
(a)
t = 5.0 s
t = 10.0 s
t = 20.0 s
t = 30.0 s
t = 80.0 s
t = 100.0 s
y (m)
x (m)
1.2
0.6
0
-0.6
-1.2
0
1
2
3
[cm]
6.00
5.69
5.38
5.07
4.76
4.45
4.14
3.83
3.52
3.21
2.89
2.58
2.27
1.96
1.65
1.34
1.03
0.72
0.41
0.20
(b)
t = 5.0 s
t = 10.0 s
t = 20.0 s
t = 30.0 s
t = 80.0 s
t = 100.0 s
[cm]
6.00
5.70
5.40
5.09
4.79
4.48
4.19
3.89
3.58
3.28
2.98
2.68
2.37
2.07
1.77
1.48
1.17
0.86
0.56
0.26

Figure 10.

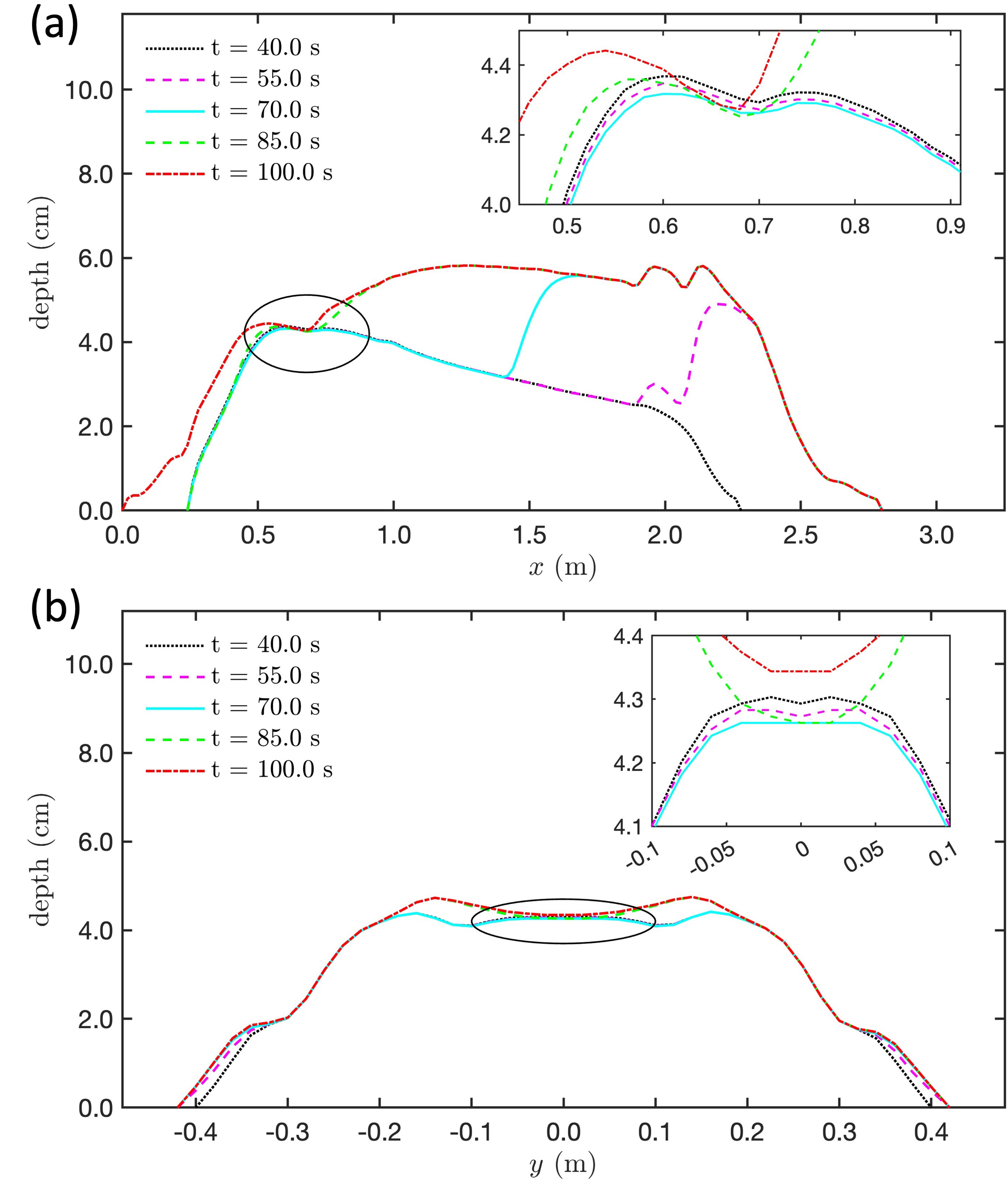
(a)
t = 40.0 s
t = 55.0 s
t = 70.0 s
t = 85.0 s
t = 100.0 s
depth (cm)
x (m)
(b)
t = 40.0 s
t = 55.0 s
t = 70.0 s
t = 85.0 s
t = 100.0 s
depth (cm)
y (m)

Figure 11.

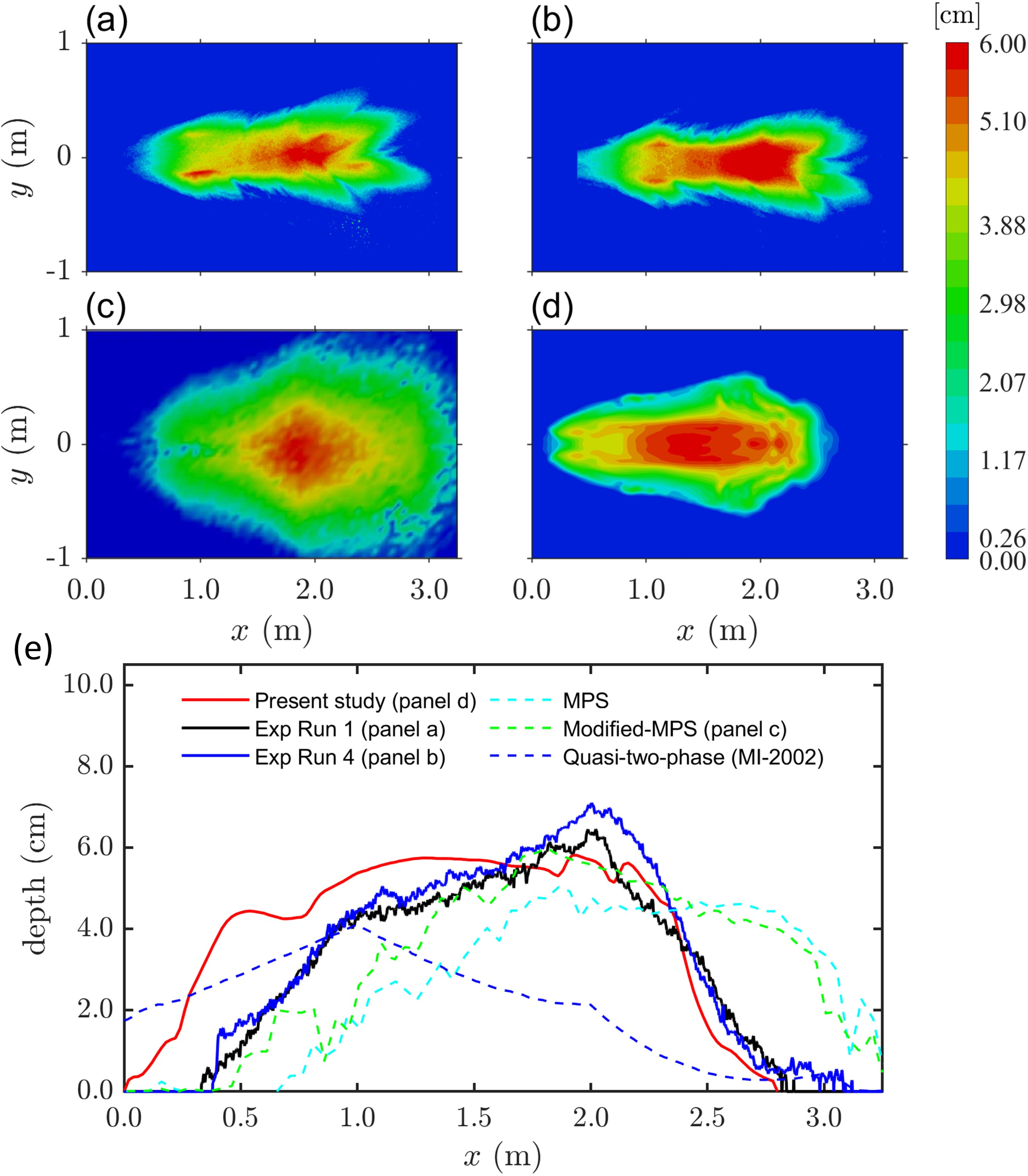
(a)
(b)
(c)
(d)
(e)
[cm]
6.00
5.10
3.88
2.98
2.07
1.17
0.26
0.00
y (m)
x (m)
1
0
-1
0.0
1.0
2.0
3.0
depth (cm)
10.0
8.0
6.0
4.0
2.0
0.0
0.5
1.5
2.5
Present study (panel d)
Exp Run 1 (panel a)
Exp Run 4 (panel b)
MPS
Modified-MPS (panel c)
Quasi-two-phase (MI-2002)